

1 **Ferruginous oceans during OAE1a and collapse of the marine sulfate pool**

2  
3  
4 Kohen W. Bauer<sup>1,2,5</sup>, Cinzia Bottini<sup>3</sup>, Sergei Katsev<sup>4</sup>, Mark Jellinek<sup>1</sup>, Roger Francois<sup>1</sup>, Elisabetta  
5 Erba<sup>3</sup>, Sean A. Crowe<sup>1,2,5,6†</sup>

6  
7 <sup>1</sup>Department of Earth, Ocean and Atmospheric Sciences,  
8 The University of British Columbia, 2207 Main Mall,  
9 Vancouver, British Columbia V6T 1Z4, Canada

10  
11 <sup>2</sup>Department of Microbiology and Immunology, Life Sciences Centre,  
12 The University of British Columbia, 2350 Health Sciences Mall,  
13 Vancouver, British Columbia, V6T 1Z3, Canada

14  
15 <sup>3</sup>Department of Earth Sciences,  
16 University of Milan, Via Mangiagalli 34,  
17 20133 Milan, Italy

18  
19 <sup>4</sup>Large Lakes Observatory and Department of Physics  
20 University of Duluth, 2205 E 5<sup>th</sup> St,  
21 Duluth, Minnesota, 55812, USA

22  
23 <sup>5</sup>Department of Earth Science  
24 The University of Hong Kong  
25 James Lee Building, Pokfulam Road, Hong Kong SAR

26  
27 <sup>6</sup>The Swire Institute of Marine Science, The University of Hong Kong, Cape d'Aguilar Road, Shek  
28 O, Hong Kong SAR

29  
30  
31  
32 †Corresponding author; sean.crowe@ubc.ca  
33  
34

35 **Highlights**

36 • Fe-speciation and redox sensitive trace element enrichment patterns in  
37 sediments from OAE1a (~120 Ma) reveal deposition under anoxic, ferruginous  
38 conditions in both the paleo-Tethys and paleo-Pacific oceans

39

40 • Widespread ferruginous ocean conditions during OAE1a are only possible with  
41 low seawater sulfate concentrations, which must have dropped well below 600  
42  $\mu\text{M}$ , and possibly below 100  $\mu\text{M}$ .

43

44 • Mass balance of the sulfur cycle predicts that pyrite burial, biomass associated  
45 organic S (bio-sulfur), and organic matter sulfurization may have played important  
46 roles as a global S-sinks during OAE1a.

47

48

49

50

51

52

53

54

55

56

57

58

59

60

61

62

63

64

65 **Abstract**

66 Seawater sulfate is one of the largest oxidant pools at Earth's surface today and  
67 its concentration in the oceans is generally assumed to have varied between 5 and  
68 28 mM since the early Phanerozoic Eon. Intermittent and potentially global  
69 Oceanic Anoxic Events (OAEs) are accompanied by changes in seawater sulfate  
70 concentrations and signal perturbations in the Earth system associated with major  
71 climatic anomalies and biological crises. Ferruginous (Fe-rich) ocean conditions  
72 developed transiently during multiple OAEs, implying strong variability in seawater  
73 chemistry and global biogeochemical cycles. The precise evolution of seawater  
74 sulfate concentrations during OAEs, however, is uncertain and thus models that  
75 aim to mechanistically link oceanic anoxia to broad-scale disruptions in the Earth  
76 system remain equivocal. Here, we use analyses of Fe-speciation and redox  
77 sensitive trace metals in slope sediments deposited in the Tethys and Pacific  
78 oceans to constrain seawater sulfate concentrations and underlying dynamics in  
79 marine chemistry during OAE1a, ~120 Ma. We find that large parts of the global  
80 oceans were anoxic and ferruginous for more than 1 million years. Calculations  
81 show that the development of ferruginous conditions requires that seawater sulfate  
82 concentrations drop below 600  $\mu\text{M}$  and possibly below 100  $\mu\text{M}$ , which is an order  
83 of magnitude lower than previous minimum estimates. Such a collapse of the  
84 seawater sulfate pool over a time scale of only one-hundred thousand years is a  
85 key and previously unrecognized feature of Phanerozoic Earth surface redox  
86 budgets. Critically, this unprecedented sensitivity has potential to dramatically alter  
87 global biogeochemical cycles, marine biology, and climate on remarkably short  
88 timescales.

89

90

91

## 92 1.0 Introduction

93 Seawater chemistry is generally thought to have evolved to its current well-  
94 oxygenated, sulfate-rich state between 540 and 420 million years ago (Ma)  
95 (Stolper and Keller, 2018). Throughout much of the preceding 3.5 billion years, the  
96 oceans were largely anoxic, predominantly Fe-rich (ferruginous), and punctuated  
97 by intervals of widespread hydrogen sulfide-rich conditions (euxinic) (Poulton and  
98 Canfield, 2011). These conditions waned in the early Phanerozoic, and thus, for  
99 much of the last 500 Myrs, marine and global biogeochemical cycles were thought  
100 to have operated much as they do today. Widespread oceanic anoxia, however,  
101 re-emerged intermittently in the Phanerozoic Eon and was particularly prevalent  
102 during warm periods such as the Cretaceous (Jenkyns, 2010). The oceans  
103 developed euxinia during some of these Oceanic Anoxic Events (OAEs) when  
104 pelagic microbial respiration was channelled through microbial sulfate reduction  
105 (MSR) producing hydrogen sulfide (H<sub>2</sub>S) that accumulated in poorly ventilated  
106 water masses (Damste and Koster, 1998; Jenkyns, 2010). Emerging evidence,  
107 however, also suggests that ferruginous conditions developed during several  
108 OAEs (OAE2, OAE3) (Marz et al., 2008; Poulton et al., 2015). Since development  
109 of ferruginous conditions hinges on the balance between Fe- and S-delivery and  
110 removal from the oceans, temporal shifts between euxinic and ferruginous  
111 conditions imply large-scale variability in ocean chemistry and the S-cycle.

112 Marine sulfate concentrations and S-isotope composition ( $\delta^{34}\text{S}_{\text{Seawater}}$ )  
113 represent a balance between the S-inputs and outputs. In the modern oceans,  
114 riverine delivery and volcanism are the main sources of sulfur to the ocean  
115 (Hansen and Wallmann, 2003). Sulfur is removed from the oceans in restricted  
116 basins by evaporite deposition, as well as in anoxic sediments and water columns  
117 through MSR, leading to pyrite formation and burial (Canfield and Farquhar, 2012).  
118 Additional, yet often overlooked, marine sulfur sinks also include biomass  
119 associated organic sulfur (bio-sulfur) and sulfurized organic matter (OM) (Canfield  
120 et al., 1998; Francois, 1987; Raven et al., 2021; Raven et al., 2018; Shawar et al.,  
121 2018). Marine organisms have molar C:S ratios of ~50 (Chen et al., 1996;  
122 Fagerbakke et al., 1996), and thus the burial flux of bio-sulfur is likely on the order

123 of 5 wt% that of organic C. Sulfurization of OM can also occur under anoxic  
124 conditions where the H<sub>2</sub>S produced during MSR reacts with OM, increasing its C:S  
125 ratio from values typical of marine biomass to as high as 8% (Eglinton et al., 1994;  
126 Raven et al., 2018). Given that reduced-S sinks expand under anoxic ocean  
127 conditions, the development of widespread oceanic anoxia during OAEs has the  
128 potential to dramatically affect the mass and isotopic composition of seawater  
129 sulfate.

130 Sulfur isotope records and analyses of fluid inclusions from the Cretaceous  
131 Period reveal that background seawater sulfate concentrations were much lower  
132 (<10 mM) than the modern oceans (28 mM) (Timofeeff et al., 2006). Episodic  
133 evaporite deposition drew seawater sulfate concentrations down even further,  
134 possibly to as low as 1 mM, during Early Cretaceous OAE1a (120 Ma) (Wortmann  
135 and Chernyavsky, 2007). This evaporite deposition likely took place intermittently  
136 both before (Davison, 2007), and after (Chaboureau et al., 2013), the event. Some  
137 stratigraphic reconstructions imply evaporite deposition contemporaneous with  
138 OAE1a (Tedeschi et al., 2017), however, this timing is not well supported by  
139 independent chronostratigraphic data. Regardless, low seawater sulfate  
140 concentrations in the Aptian oceans could have strongly influenced global  
141 biogeochemical cycling across the OAE1a interval.

142 Paleomarine sulfate concentrations have mostly been estimated through  
143 two approaches; 1) the rate method, and 2) the MSR trend method (e.g., Algeo et  
144 al. (2015), Supplementary Information), but these, importantly, do not resolve  
145 seawater sulfate concentrations below about 1 mM. The rate method estimates  
146 seawater sulfate concentrations with the product of pyrite burial fluxes and the  
147 isotopic difference between cogenetic sulfate and sulfide ( $\Delta^{34}\text{S}_{\text{Sulfate-Pyrite}}$ ) divided  
148 by the maximum rate of change in seawater sulfate  $\delta^{34}\text{S}$ . The MSR trend method  
149 is based on empirical relationships between  $\Delta^{34}\text{S}_{\text{Sulfate-Pyrite}}$  and sulfate  
150 concentrations observed in modern environments (Algeo et al., 2015). When  
151 applied to OAE1a using existing S-isotope data (Gomes et al., 2016; Kristall et al.,  
152 2018; Mills et al., 2017; Paytan et al., 2004), these methods yield estimates for  
153 seawater sulfate that are less than 1-3 mM (Fig. 1).

154           There are, however, critical limitations to estimates of seawater sulfate  
155 produced using the rate and MSR trend methods. For example, the rate method  
156 only provides maximum estimates for seawater sulfate concentrations because the  
157 measured rate of change in  $\delta^{34}\text{S}_{\text{Seawater}}$  in a given sedimentary unit is generally  
158 smaller than the calculated theoretical maximum, which is mathematically obtained  
159 when the source flux of sulfate to the oceans is zero (Algeo et al., 2015)  
160 (Supplementary Information) (Fig. 1). Since this scenario does not occur in nature,  
161 estimates provided by the rate method tend to be larger than actual seawater  
162 sulfate concentrations (Algeo et al., 2015). On the other hand, the controls on MSR  
163 and associated isotope fractionations are complex and incompletely known  
164 (Canfield and Farquhar, 2012), confounding precise application of the MSR trend  
165 method to the geologic record. Furthermore, recent work has challenged the  
166 fidelity of  $\delta^{34}\text{S}$  records in CAS and pyrite minerals, suggesting  $\delta^{34}\text{S}$  signals  
167 recorded in these mineral phases may be a function of more complex processes  
168 such as diagenetic alteration (Present et al., 2019), and often reflect local as  
169 opposed to global processes (Pasquier et al., 2021). Given these limitations, the  
170 rate and MSR trend methods are incapable of resolving seawater sulfate  
171 concentrations across the OAE1a beyond coarse maximum estimates of 1-3 mM  
172 (Fig. 1). The sensitivity of biogeochemical cycles below this range, however, is  
173 important and highlights the need for new data and models that provide more  
174 accurate and precise reconstructions of seawater sulfate concentrations during the  
175 Aptian Age.

176           Recognizing the limitations of the rate and MSR trend methods, we took a  
177 different approach to reconstructing seawater sulfate concentrations in the Aptian  
178 oceans. We studied sedimentary rocks from the Tethys (Cismon drill core) and  
179 Pacific (Deep Sea Drilling Project (DSDP) Site 463) oceans that capture OAE1a  
180 (Fig. S1). OAE1a is delineated by organic matter (OM)-rich black shale containing  
181 units that were deposited over more than a million years (Erba et al., 2010;  
182 Malinverno et al., 2010). We conducted a suite of geochemical and mineralogical  
183 analyses, which collectively reveal that OAE1a sediments were deposited under  
184 anoxic Fe-rich (ferruginous) water column conditions that extended from the

185 Tethys to the Pacific oceans and persisted for more than 1 million years. Our  
186 modeling reveals that development of these ferruginous conditions was a response  
187 to collapse of the seawater sulfate pool associated with expanded oceanic anoxia.  
188

## 189 **2.0 Methods**

### 190 *2.1 Sediment digestions and Fe-speciation analyses*

191 We worked with sedimentary rock samples from both the Cismon and  
192 DSDP Site 463 drill cores that capture OAE1a. These rocks were powdered first  
193 using an agate mill and then by hand using an agate mortar and pestle. Sample  
194 splits (200 mg) were entirely digested in a lithium metaborate fusion, using a  
195 sample to LiO<sub>2</sub> flux ratio of 1:1. Sample splits of 500 mg of sediment were  
196 subjected to a Fe-speciation sequential extraction scheme (Poulton and Canfield,  
197 2005). We also performed a revised extraction scheme that included an organic  
198 matter leach, as indicated in (Table S1). For the revised scheme our “highly  
199 reactive, Fe<sub>HR</sub>” pool is defined as carbonate-associated Fe (Fe<sub>carb</sub>, 0.5 N HCl  
200 extractable Fe), organic matter associated Fe (Fe<sub>OM</sub>), ferric (oxyhydr)oxides  
201 including magnetite (Fe<sub>Oxides</sub>, sum of dithionite and oxalate extractable Fe, Fe<sub>Goe</sub>  
202 and Fe<sub>Magnetite</sub>, Table S1), and pyrite (Fe<sub>Pyr</sub>) (Fe<sub>HR</sub> = Fe<sub>Carb</sub> + Fe<sub>OM</sub> + Fe<sub>Oxides</sub> +  
203 Fe<sub>Pyr</sub>). The Fe<sub>Tot</sub> pool is the sum of all Fe<sub>HR</sub> pools and Fe contained in silicate  
204 minerals (Fe<sub>Sil</sub>).  
205

### 206 *2.2 Elemental concentrations*

207 Extract Fe concentrations were measured by both flame atomic adsorption  
208 spectroscopy (Flame AAS, Varian 875) and inductively coupled optical emission  
209 mass spectroscopy (ICP-OES, Varian 725ES). Extract major and trace element  
210 concentrations were measured by quadrupole inductively coupled plasma mass  
211 spectroscopy (Q-ICP-MS, Perkin Elmer NexION 300D), while major elemental  
212 concentrations were determined by inductively coupled optical emission mass  
213 spectroscopy (ICP-OES, Varian 725ES). For flame AAS measurements, precision  
214 on triplicate measurements was 1.2% (1 RSD) and our limit of detection in solution  
215 was 80 µg L<sup>-1</sup>, or roughly 35 µg g<sup>-1</sup> sediment Fe, based on dilutions. For our ICP-

216 OES measurements precision on triplicate measurements for Fe was 2.2% (1  
217 RSD) and our limit of detection in solution was  $6 \mu\text{g L}^{-1}$ , or roughly  $30 \mu\text{g g}^{-1}$   
218 sediment, based on dilutions. For Al analysis via ICP-OES, precision on triplicate  
219 measurements was 1.2% (1 RSD) and our limit of detection in solution was  $6 \mu\text{g}$   
220  $\text{L}^{-1}$ , or roughly  $33 \mu\text{g g}^{-1}$ , based on dilutions. Our extractions dissolved >92% of the  
221 Fe from the PACS-2 international reference standard. Errors on Fe concentrations  
222 in the different leachates based on triplicate extractions of the PACS-2  
223 international reference standard are as follows (reported as 1 sigma RSD);  $\text{Fe}_{\text{Aca}} \pm 6.0\%$ ,  
224  $\text{Fe}_{0.5\text{NHCl}} \pm 5.8\%$ ,  $\text{Fe}_{\text{Dith}} \pm 2.8\%$ ,  $\text{Fe}_{\text{Oxa}} \pm 10.1\%$ ,  $\text{Fe}_{\text{Sil}} \pm 3.4\%$ .

225 For S analysis via ICP-OES, we achieved an RSD of <0.1% and our limit of  
226 detection was roughly  $25 \mu\text{g g}^{-1}$  sediment, based on dilutions. Total S  
227 concentrations were also determined by Bottini et al. (2012) using an elemental  
228 analyser. For our Q-ICP-MS measurements, precision on Cr was <1% (1 RSD)  
229 and our limit of detection in solution was  $0.03 \mu\text{g L}^{-1}$ , or roughly  $0.7 \mu\text{g g}^{-1}$  sediment  
230 Cr, based on dilutions. For Cr analysis via ICP-OES, we achieved an RSD of <1%  
231 and our limit of detection was roughly  $5.3 \mu\text{g g}^{-1}$  sediment, based on dilutions. For  
232 V analysis via ICP-OES, we achieved an RSD of <1% and our limit of detection  
233 was  $0.26 \mu\text{g g}^{-1}$  sediment, based on dilutions. For U and Mo analysis via Q-ICP-  
234 MS, we achieved RSDs of <1% and 3.5% respectively, and our limits of detection  
235 were roughly 0.10 and 0.40, respectively  $\mu\text{g g}^{-1}$  sediment, based on dilutions. Our  
236 fusion digestions dissolved ~100%, 97% and 100% of the Cr in the BHVO-2,  
237 MESS-3, and PACS-2 international reference standards, respectively.

238

### 239 *2.3 Microscopy and XRD*

240 Polished thin sections of the Cismon and DSDP Site 463 rocks were imaged  
241 on a Hitachi S-4800 field emission scanning electron microscope (Hitachi S-4800  
242 FEG SEM) equipped with field emission gun. Elemental concentrations were used  
243 to infer mineralogy, and these were determined by energy-dispersive X-ray  
244 spectroscopy (EDS, Oxford Instruments X-Max 80 Detector) based on X-ray  
245 fluorescence at the relevant emission energies for Fe, C, S, P, Ca and O. Sediment  
246 mineralogy was determined by powder X-ray diffraction (XRD). Rock powders



247 were mounted on non-diffracting silica plates. Continuous-scan X-ray diffraction  
248 data were collected over a range 3-90°2θ with CoKα radiation on a Rigaku Miniflex  
249 diffractometer. We analyzed the X-ray diffractograms using the International  
250 Centre for Diffraction Database PDF-4, RRUFF database, and Search-Match  
251 software by JADE. The XRD data is plotted in Figure. S2.

252

#### 253 *2.4 1D water column reactive transport model*

254 We developed a reaction transport model to explore how surface ocean  
255 sulfate concentrations influence water column sulfate drawdown and rates of pyrite  
256 deposition. This model was developed and described in detail in Crowe et al.  
257 (2014) with additional details provided in the Supplementary Information. The  
258 model predicts seawater sulfate distributions under steady-state conditions by  
259 describing changes in sulfate concentration with depth as a function of vertical  
260 transport and rates of sulfate reduction to sulfide as:

261

$$262 \quad K_z \frac{\partial^2 [SO_4^{2-}]}{\partial x^2} - R_{SR} = 0 \quad (1)$$

263

264 where  $K_z$  is the eddy diffusivity governing vertical mixing ( $m^2 d^{-1}$ ),  $x$  is the depth in  
265 the water column (m), and  $R_{SR}$  is the sulfate reduction rate ( $\mu mol m^{-3} d^{-1}$ ). For  $K_z$ ,  
266 we implemented a range of values ( $0.01 - 1 m^2 d^{-1}$ ), of which the highest value is  
267 similar to globally averaged open ocean vertical transport rates (Munk and  
268 Wunsch, 1998), and with lower values representing more strongly stratified seas  
269 (Table S2). Sulfate reduction rates were calculated with a Michaelis-Menten like  
270 kinetic description:

271

$$272 \quad R_{SR} = \frac{V_{max} [SO_4^{2-}]}{K_m + [SO_4^{2-}]} \quad (2)$$

273

274 where  $K_m$  is the half-saturation constant ( $\mu M$ ). For  $K_m$ , we considered a range of  
275 values from 3.6 to 450  $\mu M$ , which are characteristic of organisms from modern  
276 environments with both high and low seawater sulfate concentrations (Table S2).

277  $V_{max}$  is the maximum rate of sulfate reduction ( $\mu\text{mol m}^{-3} \text{d}^{-1}$ ), when sulfate supply  
278 is unlimited, and thus corresponds to the scenario when sulfate reduction is limited  
279 by organic matter availability.  $V_{max}$  can, therefore, be estimated based on models  
280 of organic matter degradation rates in modern anoxic marine systems. We thus  
281 parameterized  $V_{max}$  according to carbon degradation rates in the modern ocean  
282 under both high ( $V_{max} = 15 \mu\text{M yr}^{-1}$ ) and low productivity ( $V_{max} = 1 \mu\text{M yr}^{-1}$ ) scenarios  
283 (Crowe et al., 2014; Hartnett and Devol, 2003) (Table S2).

284 We set two conditions that tether our 1D model reconstructions for seawater  
285 sulfate to the rock record: 1) S-burial burial fluxes (pyrite, total sulfur ( $S_{\text{Tot}}$ )) were  
286 used to place limits on total net sulfide production fluxes, which cannot be greater  
287 than the total-reduced S-burial fluxes recorded in OAE1a sediments assuming all  
288 net  $\text{H}_2\text{S}$  produced is quantitatively converted to the sediment; and 2) under  
289 ferruginous conditions, seawater sulfate concentrations must be quantitatively  
290 drawn down to preserve appreciable non-pyritized  $\text{Fe}_{\text{HR}}$  in the presence of  
291 abundant reactive OM. This is because in sediments that contain reactive OM,  
292 sulfate is used by sulfate reducing microorganisms to produce  $\text{H}_2\text{S}$  and production  
293 of this  $\text{H}_2\text{S}$  will cause the pyritization of  $\text{Fe}_{\text{HR}}$  until the  $\text{Fe}_{\text{HR}}$  pool is completely  
294 pyritized, sulfate is exhausted, and/or the reactive OM is exhausted. Sulfur burial  
295 fluxes were calculated by combining sedimentation rates (Malinverno et al., 2010)  
296 with pyrite and  $S_{\text{Tot}}$  concentrations in the Cison and DSDP Site 463 sediments.  
297 Together, these two conditions place upper limits on the maximum sulfate flux that  
298 can be converted to pyrite through MSR and reaction of the  $\text{H}_2\text{S}$  produced with  
299  $\text{Fe}_{\text{HR}}$ . We thus use our model to identify a parameter space of possible upper  
300 bounds for seawater sulfate concentrations.

301

### 302 *2.5 Sulfur mass balance model*

303 To connect the results of our reactive transport modeling to the requisite  
304 dynamics in the global sulfur cycle we developed a box model following published  
305 studies (Gomes et al., 2016; Mills et al., 2017). Through a system of coupled  
306 evolution equations, we track the mass and isotopic composition of marine sulfate

307 as a function of sources and sinks of sulfur to and from the ocean using the  
308 following equations;

309

$$310 \quad \frac{\partial M_S}{\partial t} = F_w + F_h - (F_{pyr} + F_{sulf} + F_{evap} + F_{OM} + F_{CAS}) \quad (3)$$

311

$$312 \quad \frac{\partial \delta^{34}S_{sulphate}}{\partial t} = ((F_w \delta_w + F_h \delta_h) - \delta^{34}S_{sulphate}(F_w + F_h) - F_{pyr} \Delta^{34}S_{pyr} - F_{sulf} \Delta^{34}S_{sulf}) / M_S \quad (4)$$

313

314 Here,  $M_S$  is the mass of sulfur in the ocean;  $F_H$ ,  $F_W$ , are the volcanic (including  
315 hydrothermal), and weathering input fluxes of S, respectively;  $F_{pyr}$ ,  $F_{sulf}$ ,  $F_{OM}$ ,  $F_{CAS}$   
316 and  $F_{evap}$  are the burial fluxes of pyrite, sulfurized-OM, bio-sulfur, carbonate  
317 associated sulfate, and evaporites, respectively.  $\delta^{34}S_{Sulfate}$  is the S-isotope  
318 composition of seawater sulfate.  $\delta_w$  and  $\delta_h$  are the S-isotope composition of the  
319 weathering (5.2‰) and volcanic (3.2‰) inputs respectively,  $\Delta^{34}S_{pyr}$  is the average  
320 isotope separation factor associated with pyrite deposition ( $37 \pm 10\%$ ), which is  
321 based on the difference between seawater sulfate and contemporaneously  
322 deposited pyrite in the modern oceans (Hansen and Wallmann, 2003).  $\Delta^{34}S_{Sulf}$  is  
323 the average isotope separation factor associated with sulfurized-OM ( $15 \pm 5\%$ )  
324 (Raven et al., 2018). To obtain an initial value for  $M_S$ , we assume an ocean volume  
325 of  $1.38 \times 10^{18} \text{ m}^3$  and an initial sulfate concentration of 4 mM, in accordance with  
326 Cretaceous estimates similar to previous modeling work (Gomes et al., 2016;  
327 Wortmann and Chernyavsky, 2007). We take  $\delta^{34}S_{Sulfate} = 20.2\%$  as an initial value,  
328 which is within error of measurements of pre-OAE1a  $\delta^{34}S_{Sulfate}$ . From these initial  
329 conditions, we establish a pre-OAE1a steady-state condition (Table S4). Additional  
330 details can be found in the Supplementary Information.

331

## 332 **3.0 Results**

### 333 *3.1 Fe-speciation*

334 Fe-speciation analyses reveal enrichments of pyritizable Fe ( $Fe_{HR}$ ) across  
335 the OM-rich shale intervals that define OAE1a in both Cismon and DSDP Site 463  
336 rocks (Fig. 2), relative to rocks stratigraphically above and below. We note that  
337 these enrichments are not due to dilution effects by  $CaCO_3$  contents in pre- and

338 post-event rocks. Ratios of  $Fe_{HR}/Fe_{Tot} > 0.38$  imply sediment deposition beneath  
339 anoxic waters if ratios of  $Fe_{Tot}/Al$  are also  $> 0.5$  and  $C_{org}$  contents are  $> 0.5$  wt%  
340 (Raiswell et al., 2018).  $Fe_{HR}/Fe_{Tot}$  values recorded in the Cismon core during  
341 OAE1a are consistently above 0.38 and have  $Fe_{Tot}/Al > 0.5$  as well as  $C_{org} > 0.5$   
342 wt%, diagnostic of deposition below an anoxic water column (Fig. 3).  $Fe_{HR}/Fe_{Tot}$   
343 ratios in rocks that bound OAE1a have  $Fe_{HR}/Fe_{Tot} < 0.38$  (Fig. 3). Similarly,  
344  $Fe_{HR}/Fe_{Tot}$  ratios in rocks deposited at DSDP Site 463 also capture intervals with  
345 values  $> 0.38$  and  $Fe/Al > 0.5$  and  $C_{org} > 0.5$  wt%. However, some  $Fe_{HR}/Fe_{Tot}$  values  
346 in sediments deposited during OAE1a at DSDP Site 463, are below the  
347  $Fe_{HR}/Fe_{Tot} > 0.38$  threshold (Fig. 3). The sediments deposited during OAE1a, at  
348 both sites studied, also preserve appreciable non-pyritized  $Fe_{HR}$  (Fig. 2).  
349  $Fe_{Pyr}/Fe_{HR}$  ratios are a direct measure of the degree of pyritization of the highly  
350 reactive  $Fe_{HR}$  pool and ratios  $< 0.7$  indicate deposition under a ferruginous water  
351 column with excess highly reactive Fe (Raiswell et al., 2018). All rocks deposited  
352 at the Cismon and DSDP 463 sites during the OAE1a interval have  
353  $Fe_{Pyr}/Fe_{HR} \ll 0.7$  (Fig. 3).

354 The 0.5 N HCl leach selectively dissolves poorly crystalline Fe (oxyhydr)-  
355 oxides, reactive Fe-carbonates, and acid volatile sulfide (AVS). Determination of  
356 both Fe(II) and Fe(III) in the 0.5 N HCl leach, therefore, provides a means of further  
357 speciating Fe between highly reactive Fe(II) and Fe(III) phases, as well as  
358 determining the association of other elements, like P, with these phases. We find  
359 that there was detectable Fe(III) in most of the 0.5 N HCl extracts (Fig. S3), but  
360 that this Fe(III) represented a very small component of the total highly reactive Fe  
361 in the sediments. For Cismon sediments this translates to an average of  $\sim 0.5\%$  of  
362 the  $Fe_{HR}$  pool. For DSDP Site 463 sediments this translates to an average of  $\sim 2.0\%$   
363 of the  $Fe_{HR}$  pool (Fig. S3). Furthermore, we observe that on average only 7% and  
364 5% of the total P is associated with poorly crystalline Fe-(oxyhydr)-oxide phases  
365 in the Cismon and DSDP Site 463 sediments, respectively (Fig. S3).

366

367 *3.2 Redox sensitive trace elements (RSTEs)*

368 Multiple redox sensitive trace elements (RSTEs) display strong enrichments  
369 relative to the Post Archean Average Shale (PAAS) reference material (McLennan,  
370 2001). Rhenium is highly enriched in OAE1a sediments (Fig. 4), with average Re  
371 concentrations of 100 and 2.0 ng g<sup>-1</sup> in the Cismon and DSDP Site 463 cores,  
372 respectively. Average Re concentrations in rocks that bound OAE1a are 1.0 and  
373 1.0 ng g<sup>-1</sup> in the Cismon and DSDP Site 463 cores, respectively (Fig. 3). During  
374 OAE1a average shale normalized Re enrichment factors (Re<sub>EF</sub>) are 746 and 18 in  
375 the Cismon and DSDP Site 463 cores, respectively. Average Re<sub>EF</sub> in rocks that  
376 bound OAE1a are 15 and 21 in the Cismon and DSDP Site 463 cores, respectively  
377 (Fig. 4). During OAE1a Cr enrichment factors (Cr<sub>EF</sub>) are 5.0 and 4.0 in the Cismon  
378 and DSDP Site 463 cores, respectively. Average Cr<sub>EF</sub> in rocks that bound OAE1a  
379 are 3.9 and 1.1 in the Cismon and DSDP Site 463 cores, respectively (Fig. 4).  
380 During OAE1a average V enrichment factors (V<sub>EF</sub>) are 2.5 and 1.7 in the Cismon  
381 and DSDP Site 463 cores, respectively. Average V<sub>EF</sub> in rocks that bound OAE1a  
382 are 1.1 and 1.3 in the Cismon and DSDP Site 463 cores, respectively (Fig. 4). In  
383 addition to our new RSTE data, and in contrast to Re, V, and Cr, a compilation of  
384 Mo concentrations in sediments deposited across OAE1a (Charbonnier et al.,  
385 2018; Follmi, 2012; Westermann et al., 2013) shows that only 2 out of 196 samples  
386 analysed have Mo concentrations greater than the 25 µg g<sup>-1</sup>, a threshold that  
387 implies deposition under euxinic conditions (Lyons and Severmann, 2006) (Fig.  
388 4e).

389

### 390 3.3 Microscopy and XRD

391 In both the Cismon and DSDP Site 463 sediments, the presence of Fe<sub>HR</sub> is  
392 demonstrable through X-ray diffraction analyses (Fig. S2). An appreciable fraction  
393 of this Fe<sub>HR</sub> is preserved as Fe<sub>Carb</sub> (0.1 – 0.3 wt%) (Supplementary Data), which  
394 operationally reflects the mineral siderite (Fig. S2). In thin section, pyrite/marcasite  
395 crystals in the Cismon and DSDP Site 463 rocks are well-preserved, lacking  
396 evidence of oxidation rims, dissolution pitting, or pervasive cracking (Fig. 5). A  
397 collection of images of consistently well-preserved pyrite/marcasite (including  
398 framboids) from multiple thin sections are broadly representative of the OAE1a

399 sediments (Fig. 5). Additionally, electron micrographs and corresponding SEM-  
400 EDS analyses reveal pristine Ca-P-rich minerals (apatite) and demonstrate a much  
401 stronger association of P with Ca than Fe (Fig. 5).

402

### 403 *3.4 1D water column reaction transport modeling*

404 Results from the water-column reactive transport modeling illustrate how  
405 sulfate drawdown and pyrite burial fluxes scale as a function of surface ocean  
406 sulfate concentrations. These calculations yield estimates for seawater sulfate that  
407 must be less than ~600  $\mu\text{M}$ , and less than 100  $\mu\text{M}$  under most scenarios (Fig. 6).  
408 A sensitivity analysis of our model and its relevant parameters ( $V_{max}$ ,  $K_m$  and  $K_z$ )  
409 provides constraints on allowable seawater sulfate concentrations that fulfill  
410 conditions that sulfate concentrations be drawn down to negligible levels (condition  
411 1, Methods section 3.4) without exceeding the pyrite/ $S_{\text{Tot}}$  burial rates recorded in  
412 the OAE1a sediments (condition 2, Methods section 3.4). Higher values of  $K_m$   
413 result in lower rates of sulfate reduction and S-burial. Higher values for  $V_{max}$  result  
414 in high rates of sulfate reduction and S-burial. The  $K_z$  values used are conservative  
415 with respect to sulfate concentrations as higher values for  $K_z$  lead to lower possible  
416 surface seawater sulfate concentrations (Fig. 6) (Table S2). In general, the  
417 scenario which leads to the maximum predicted seawater sulfate concentration  
418 (~600  $\mu\text{M}$ ) corresponds to  $V_{max}$  values similar to respiration rates in modern anoxic  
419 water columns (~7  $\mu\text{M yr}^{-1}$ ), high  $K_m$  (450  $\mu\text{M}$ ), and slightly more sluggish vertical  
420 mixing ( $K_z$ , 0.1  $\text{m}^{-2} \text{d}^{-1}$ ) relative to the modern open oceans (Fig. 6) (Table S2). All  
421 other scenarios that satisfy model conditions 1 and 2 (Section 2.4) yield lower  
422 seawater sulfate concentrations.

423

### 424 *3.5 Sulfur mass-balance model*

425 Global sulfur mass balance modeling reveals that low  $\mu\text{M}$  seawater sulfate  
426 concentrations during OAE1a are supported by existing constraints on global S-  
427 budgets and S-isotope data. A perturbation to the global S-cycle lasting roughly  
428 0.5 Myrs led to enhanced volcanic and riverine S-inputs (Mills et al., 2017) of  $\sim 2.3$   
429  $\pm 0.6 \text{ Tmol yr}^{-1}$  and  $\sim 3.1 \pm 0.8 \text{ Tmol yr}^{-1}$ , respectively (Fig. 8), assuming a

430 conservative ~25% uncertainty for the different S-fluxes (Canfield and Farquhar,  
431 2012). To both balance these enhanced S-inputs and draw seawater sulfate down  
432 to concentrations that satisfy the 1D modeling results (Fig. 6), requires S-burial  
433 fluxes of  $6.5 \pm 0.5 \text{ Tmol yr}^{-1}$  (95% confidence interval, Fig. S7). The Aptian S-  
434 isotope record, furthermore, is satisfied, within the uncertainties of Cretaceous S-  
435 fluxes (Table S4), when oceanic S-removal fluxes are appropriately distributed  
436 between pathways that are strongly isotopically fractionated from seawater (i.e.,  
437 pyrite, sulfurized-OM), and those that are not (i.e., evaporites and bio-sulfur, Fig.  
438 8). Following OAE1a, the seawater sulfate pool can rebound to mM sulfate  
439 concentrations on timescales of ~1 Myrs through a reduction in S-removal fluxes  
440 and the continued supply of S through volcanism and weathering that is largely  
441 unchanged over this time scale (Jellinek et al., 2020) (Fig. 8).

442

## 443 **4.0 Discussion**

### 444 *4.1 Sample fidelity*

445 The OAE1a rocks we analyzed from both Cismon and DSDP 463 appear  
446 pristine with little evidence for post-depositional oxidation. Previous work observed  
447 extensive pyrite oxidation during storage of OAE sediments (OAE2, Kraal et al.,  
448 2009). We thus assessed potential post-depositional oxidation through detailed  
449 optical and electron microscopy, focusing on observations of pyrite/marcasite  
450 crystal morphology and texture along cracks, or near sample edges where pyrite  
451 grains are most exposed to the atmosphere. Visually, all pyrite/marcasite grains  
452 observed in both cores appear well-preserved (Fig. 5) with no evidence of post-  
453 depositional oxidation. We also observe pristine Ca-P-rich minerals and limited  
454 association of P with Fe (Fig. 5). Pyrite/marcasite oxidation can cause dissolution  
455 of Ca-P minerals and a redistribution of P into newly formed Fe-(oxyhydr)oxide  
456 minerals (Kraal et al., 2009). Thus, the preservation of Ca-P-rich minerals in our  
457 samples and lack of Fe-associated P further implies negligible oxidation artifacts  
458 (Supplementary Information).

459 Tests for more subtle effects of post depositional alteration based on  
460 geochemical information support microscopic observations and demonstrate

461 negligible oxidation of sediment Fe-species. Key Fe- and S-bearing minerals  
462 sensitive to oxidation include acid volatile S-minerals (AVS), pyrite, and/or siderite.  
463 Recognizing that the initial product of acid volatile S (AVS), pyrite, and/or siderite  
464 oxidation is poorly crystalline Fe (oxyhydr)-oxides (Luther III et al., 1982), such  
465 oxidation would be observed as 0.5 N HCl leachable Fe(III). Most Fe leached in  
466 0.5 N HCl was Fe(II) and the concentration of 0.5 N HCl leachable Fe(III) in all  
467 rocks analyzed was a negligible (<2%) component of the total Fe<sub>HR</sub> (Fig. S3).  
468 Importantly, 0.5 N HCl leachable Fe(III) is not expected to be preserved in anoxic,  
469 OM-rich sediments, and the Fe(III) we measured in this fraction may thus be the  
470 product of very limited post depositional oxidation. Critically, however, such a small  
471 amount of post depositional oxidation has a negligible effect on our Fe-speciation  
472 results and their interpretation (Fig. S4), as we show in detail below.

473 The conversion of both pyrite and siderite to Fe (oxyhydr)-oxides during  
474 sample oxidation can cause a redistribution of Fe from Fe<sub>Pyr</sub> and Fe<sub>Carb</sub> to Fe<sub>Ox</sub>.  
475 Because these pools are summed in the Fe<sub>HR</sub> pool, oxidation has little potential to  
476 influence the Fe<sub>HR</sub>/Fe<sub>Tot</sub> or Fe/Al ratios, that are used to discriminate between oxic  
477 versus anoxic conditions. However, Fe-speciation discriminates between  
478 ferruginous and euxinic conditions based on Fe<sub>Pyr</sub>/Fe<sub>HR</sub>, with ferruginous conditions  
479 indicated at conservative ratios <0.7. Given that pyrite oxidation decreases this  
480 ratio, it has potential to obscure signals for euxinia. We thus tested our capacity to  
481 accurately discriminate between ferruginous and euxinic conditions based on  
482 Fe<sub>Pyr</sub>/Fe<sub>HR</sub> ratios measured in our samples by fully unpacking the wealth of  
483 information in Fe-speciation analyses (Fig. S4). As one example, we summed  
484 Fe<sub>Ox</sub>, the product of Fe<sub>Pyr</sub> oxidation, with Fe<sub>Pyr</sub> to come up with a maximum possible  
485 'pre-oxidation' ratio, Fe'<sub>Pyr</sub>/Fe<sub>HR</sub>. Fe'<sub>Pyr</sub>/Fe<sub>HR</sub> ratios in both the Cismon and DSDP  
486 Site 463 sediments are nearly all below the conservative <0.7 threshold for the  
487 delineation of ferruginous conditions (Fig. 3). As a further example, we assumed  
488 all the sulfur present in the sediment was originally pyrite and calculate  
489 conservative pyritized Fe values (S<sub>Tot</sub>/Fe<sub>HR</sub>). We find that most of these values are  
490 also below the conservative threshold of 0.7 in both the Cismon and DSDP Site  
491 463 sediments (Fig. S4). We employed an additional 3 tests (Supplementary



492 Information) and together these all demonstrate that our Fe-speciation analyses  
493 are robust, and that sample oxidation had negligible, if any, effect on our ability to  
494 discriminate between euxinic and ferruginous conditions (Fig. S4).

495

#### 496 *4.2 Anoxic ferruginous conditions*

497 Fe-speciation in sediments deposited at both the Cismon and DSDP Site  
498 463 sites records deposition under anoxic, ferruginous water column conditions  
499 (Fig. 3). Ratios of  $Fe_{HR}/Fe_{Tot} > 0.38$  in all the Cismon sediments deposited during  
500 OAE1a are diagnostic of anoxic conditions in the Tethys Ocean. Some  $Fe_{HR}/Fe_{Tot}$   
501 values in sediments deposited during OAE1a at DSDP Site 463, however, are  
502 below the threshold ( $>0.38$ ) used to diagnose anoxia and are thus ambiguous to  
503 depositional redox state based on Fe-speciation alone. We note, however, that Fe-  
504 speciation analyses cannot diagnose sediment deposition under oxic conditions.  
505 This is because of Fe mass-balance, which dictates that enrichment of  $Fe_{HR}$  at one  
506 depositional location by necessity requires its depletion in another. Some  
507 sediments must, therefore, act as a source of  $Fe_{HR}$ . It follows that  $Fe_{HR}/Fe_{Tot}$  ratios  
508  $< 0.38$  can also result from deposition beneath an anoxic water column and such  
509 ratios signify that the strength of the Fe-shuttle, and Fe-delivery to the open Pacific  
510 Ocean (DSDP Site 463), likely waxed and waned throughout OAE1a. In contrast,  
511 continental slope sediments, like those deposited at the Tethys site (Cismon core),  
512 likely served as more persistent and effective oceanic sinks for  $Fe_{HR}$ .

513 Sediments deposited during OAE1a at both sites preserve appreciable non-  
514 pyritized  $Fe_{HR}$ , which thus signals deposition and burial in a sulfide-poor,  
515 ferruginous setting.  $Fe_{Pyr}/Fe_{HR}$  in sediments from both sites fall well below (average  
516  $Fe_{HR}/Fe_{Pyr} = 0.12$ ) the conservative threshold of 0.7 for diagnosis of euxinic  
517 conditions. Values  $< 0.7$  are due to preservation of non-pyritized  $Fe_{HR}$  and, by  
518 definition, such values require insufficient  $H_2S$  supply to pyritize the available  $Fe_{HR}$ ,  
519 and this thus also precludes accumulation of free  $H_2S$  and the development of  
520 euxinia. Organic matter, however, can provide an additional sink for  $H_2S$  through  
521 sulfurization reactions that can compete with  $Fe_{HR}$  for reaction with available  $H_2S$ ,  
522 possibly leading to the deposition of non-pyritized  $Fe_{HR}$  (Raven et al., 2021b). Note

523 for example, that sulfurization reactions are appreciable in the modern Eastern  
524 Tropical North Pacific (ETNP) water column (Raven et al., 2021b), however, in this  
525 sulfate-rich modern setting, MSR proceeds in the underlying sediment with the  
526 ultimate effect of pyritizing almost all  $Fe_{HR}$  ( $Fe_{HR}/Fe_{Pyr} = 0.6$ ) on diagenetic  
527 timescales (Eroglu et al., 2021). Likewise, while sulfurization hasn't been  
528 measured explicitly in euxinic environments like the Cariaco Basin or Black Sea,  
529 one would expect it to be extensive there, and yet MSR-driven diagenesis is  
530 extensive in the underlying sediment, driving near complete pyritization of  $Fe_{HR}$   
531 (Hardisty et al., 2018; Raiswell and Canfield, 1998). These classic examples form  
532 the basis of the Fe-speciation proxy and given that sulfurization operates in these  
533 modern systems, it is implicit in the proxy. Values of  $Fe_{Pyr}/Fe_{HR}$  far less than 0.7  
534 preserved in sediments that contain abundant OM deposited under anoxic  
535 conditions ( $Fe_{HR}/Fe_{Tot} > 0.38$ ), therefore, either reflect sulfate depletion and  
536 deposition from a sulfate and sulfide poor water column, or lack of sulfide  
537 production from available sulfate, which we revisit below.

538 The distribution of RSTEs in sediments from both the Cismon and DSDP  
539 463 sites also reveals deposition under anoxic, ferruginous conditions. Rhenium is  
540 highly enriched in OAE1a sediments, and this confirms deposition under anoxic  
541 conditions at both sites given tendency for Re enrichment under both ferruginous,  
542 and to a lesser degree euxinic conditions (Tribovillard et al., 2006) (Fig. 3).  
543 Deposition under euxinic conditions is often accompanied by strong Mo  
544 enrichments and deposition under euxinic conditions can be conditionally inferred  
545 when sedimentary Mo concentrations are  $>25 \mu g g^{-1}$  (Lyons and Severmann,  
546 2006). However, most OAE1a samples analysed here have a conspicuous lack of  
547 Mo enrichment with correspondingly strong enrichments in other RSTEs (V, Cr,  
548 Re) (Fig. 4). This supports the Fe-speciation data and diagnoses the deposition of  
549 sediments at the Cismon and DSDP 463 sites under ferruginous, rather than  
550 euxinic conditions.

551 Our conclusion for deposition of OAE1a sediments under ferruginous  
552 conditions is underscored by comparisons of RSTE distributions in OAE1a  
553 sediments and those deposited in euxinic regions in the modern oceans. Strikingly,

554 the general pattern of RSTE enrichments (Cr, V, Re) with lack of corresponding  
555 Mo enrichment in the OAE1a sediments, strongly contrasts observations from  
556 modern euxinic sediments (Bennett and Canfield, 2020) (Fig. 7). This can be seen  
557 when enrichment factors (EF) of these RSTEs are normalized to  $Mo_{EF}$  in the  
558 OAE1a sediments and compared to ratios of  $RSTE_{EF}/Mo_{EF}$  in example modern  
559 euxinic basins (Fig. 7). Most strikingly, Cr, V, and Re are on average 150, 50, and  
560 10 times more enriched in the OAE1a sediments than in modern euxinic  
561 sediments, relative to Mo, respectively (Fig. 7). Furthermore, concentrations of Mo  
562  $>25 \mu g g^{-1}$ , sporadically observed in some OAE1a sediments from other sites (Fig.  
563 4e), need not reflect deposition from euxinic waters. Instead, such enrichments  
564 can be achieved through a variety of processes and given the Fe-speciation and  
565 OM contents of OAE1a sediments, likely reflect Fe-oxide and OM-Mo shuttling to  
566 the sediment (Hardisty et al., 2018). We note that development of global euxinia  
567 for a brief interval at the initiation of OAE1a, and/or hydrological restriction and  
568 reservoir effects, have potential to induce widespread drawdown in seawater  
569 RSTE inventories (Tribouillard et al., 2006), possibly contributing to muted  $Mo_{EF}$ .  
570 Such drawdown, however, doesn't explain the broader pattern of RSTE  
571 distributions given that several non-Mo RSTEs are strongly enriched. Instead, the  
572 RSTE enrichment patterns of OAE1a sediments must reflect pervasive anoxic  
573 conditions throughout OAE1a and given known mechanisms for differential RSTE  
574 enrichments, and our Fe-speciation results, the enrichments in Cr, V, and Re are  
575 best explained by deposition from ferruginous oceans.

576

#### 577 *4.3 Surface-ocean sulfate scarcity during OAE1a*

578 In OM-rich settings, like those that supported deposition of OAE1a  
579 sediments, residual sulfate is incompatible with  $Fe_{Pyr}/Fe_{HR} < 0.7$ . This is because  
580 under anoxic conditions, available OM supports sulfate reduction and  
581 corresponding sulfide production until either sulfate or OM is exhausted.  
582  $Fe_{Pyr}/Fe_{HR} < 0.7$  can develop in scenarios where there is insufficient OM to fuel  
583 sulfate reduction, as is the case in many modern hydrothermal sediments (e.g.,  
584 Southeast Pacific Rise (SEPR)), which are different than the sediments deposited

585 during OAE1a. The two scenarios can be easily distinguished by both the sediment  
586 OM content (e.g., OAE1a >8 wt%, SEPR <0.01 wt%), and by the speciation of non-  
587 pyritized Fe<sub>HR</sub>. Given that OM is abundant (0.1 - 8.0 wt%) in OAE1a sediments,  
588 sulfate reduction and resulting pyritization of Fe<sub>HR</sub> during deposition of OAE1a  
589 sediments was unlikely to have been OM-limited, and instead was almost certainly  
590 sulfate limited. Recognizing that OM-sulfurization can lead to a decrease in OM  
591 reactivity (Raven et al., 2021b), we considered the possibility that the 0.1 - 8.0 wt%  
592 residual OM in the OAE1a sediment was rendered 'non-reactive' through  
593 sulfurization, such that diagenesis ceased, and sulfate persisted without  
594 supporting MSR. We view this as unlikely, however, given that an abundance of  
595 observations in modern anoxic systems, like under OMZs, in the Black Sea, or  
596 Cariaco Basin, where sulfurization should be extensive, support extensive MSR-  
597 driven diagenesis, even to the point of sulfate exhaustion and CH<sub>4</sub> production.

598         Appreciable OM in anoxic sediment tends to fuel reduction of Fe<sub>HR</sub> and  
599 conversion of ferric (oxyhydr)-oxide phases to minerals like siderite and magnetite,  
600 whereas lack of OM tends to preserve ferric (oxyhydr)-oxides as minerals like  
601 goethite or hematite, as in the goethite dominated sediments of the SEPR (Poulton  
602 and Canfield, 2006). Our conclusion is underscored by the considerable fraction  
603 of Fe<sub>HR</sub> preserved as Fe<sub>Carb</sub>, which operationally reflects the mineral siderite, the  
604 presence of which was also unambiguously demonstrated through X-ray diffraction  
605 analyses (Fig. S2). Notably, the preservation of siderite also requires depletion of  
606 sulfate since siderite is rapidly ( $t_{1/2} = 22$  minutes) converted to pyrite when exposed  
607 to H<sub>2</sub>S (Berner, 1981; McAnena, 2011). All rocks deposited at the Cismon and  
608 DSDP 463 sites during the OAE1a interval have Fe<sub>Pyri</sub>/Fe<sub>HR</sub> <0.7, and host  
609 appreciable Fe(II)<sub>HR</sub> phases. The concurrent preservation of abundant  
610 sedimentary OM and non-pyritized Fe(II)<sub>HR</sub> thus demonstrates that pyritization was  
611 limited by sulfate availability and implies sulfate drawdown to negligible  
612 concentrations.

613         Surface ocean seawater sulfate concentrations were below 600  $\mu$ M and  
614 potentially less than 100  $\mu$ M during the deposition of OAE1a sediments. Using  
615 rates of MSR and physical transport parameterized based on modern marine

616 organisms and ecosystems (Table S2), 1D water-column modeling across  
617 scenarios that capture the entire possible parameter space yields estimates for  
618 seawater sulfate that were less than ~600  $\mu\text{M}$  in all scenarios, and less than 100  
619  $\mu\text{M}$  under most reasonable scenarios (Fig. 6). Importantly, imposing higher sulfate  
620 concentrations in this model with realistic transport across oceanic pycnoclines  
621 and sediment accumulation rates, yields pyrite burial fluxes much higher than  
622 those recorded in OAE1a sediments (conservative maximum =  $10 \text{ mmol m}^{-2} \text{ yr}^{-1}$ )  
623 (Fig. 6). Other parameter values at higher sulfate concentrations and appropriately  
624 low pyrite burial rates leave residual sulfate in the water column and are thus  
625 incompatible with the preservation of non-pyritized  $\text{Fe(II)}_{\text{HR}}$ , in OM-rich sediments,  
626 and sediment deposition under ferruginous conditions (Fig. 6).

627

#### 628 *4.4 Seawater sulfate dynamics in the Aptian age*

629 Our observation of ferruginous conditions during OAE1a requires a decline  
630 of the seawater sulfate pool from low mM to hundreds of  $\mu\text{M}$  concentrations over  
631 an interval on the order of 50 kyrs, commensurate with the rapid onset of  
632 ferruginous conditions during OAE1a, as delineated by the Fe-speciation and C-  
633 isotope records (Fig. 2). Seawater sulfate concentrations were drawn down to as  
634 low as 1 mM preceding OAE1a as the result of evaporite deposition (Wortmann  
635 and Chernyavsky, 2007). Evaporite deposition effectively draws sulfate down to 1  
636 mM, but when sulfate concentrations drop below 1 mM, seawater saturation with  
637 respect to sulfate-minerals (gypsum) during evaporation requires unrealistically  
638 high  $\text{Ca}^{2+}$  concentrations that are inconsistent with Aptian seawater chemistry  
639 (Timofeeff et al., 2006) (Fig. S5). Our observation of ferruginous conditions and  
640 sub-mM surface ocean seawater sulfate concentrations thus effectively rule out  
641 the deposition of OM-rich shales at the same time as the formation of evaporites  
642 containing abundant gypsum. This requires that evaporitic gypsum deposition  
643 likely took place before the OAE1a interval, in the Late Barremian to early Aptian,  
644 as previously considered (Davison, 2007). Seawater sulfate drawdown to <600  
645  $\mu\text{M}$ , instead, requires a second phase of sulfate sequestration through MSR and  
646 reduced-S burial. Expansion of the pyrite and sulfurized-OM sinks during OAE1a

647 provides a plausible mechanism to lower seawater sulfate concentrations and  
648 drive subsequent development of ferruginous conditions.

649         Enhanced pyrite burial and sulfurized-OM associated with expansion of  
650 oceanic anoxia offsets strong hydrothermal and weathering inputs of S to the  
651 oceans during OAE1a and contributes to sulfate drawdown. Sulfur mass balance  
652 modeling reveals that an increase in global pyrite deposition rates from 0.66 to a  
653 maximum of  $1.15 \pm 0.30$  Tmol yr<sup>-1</sup> in conjunction with an increase in sulfurized-OM  
654 burial of  $3.15 \pm 0.80$  Tmol yr<sup>-1</sup> (Fig. 8), partly offsets enhanced S-inputs and  
655 contributes to sulfate drawdown, while remaining consistent with the S-isotope  
656 record (Fig. 8). Pyrite and sulfurized-OM deposition rates are higher under anoxic  
657 conditions and indeed pyrite and OM burial was greatly enhanced during OAE1a  
658 (Fig. 2). Such enhanced pyrite and sulfurized-OM burial could be achieved by  
659 expanding the global extent of water column anoxia. For instance, if water column  
660 anoxia expanded from 0.1%, its extent in the modern ocean (Martin et al., 1987),  
661 to up to ~10%, the increase from 0.66 to 1.15 Tmol yr<sup>-1</sup> could be achieved with  
662 area specific pyrite deposition rates of 35 mmol m<sup>-2</sup> yr<sup>-1</sup> in regions of ocean anoxia,  
663 which is similar to rates of pyrite burial in sediments underlying modern OMZs (Fig.  
664 6 and Fig. S6). Likewise, under anoxic ocean conditions, available evidence  
665 suggests maximum H<sub>2</sub>S uptake by OM between ~3-8% (Eglinton et al., 1994;  
666 Raven et al., 2018). OM burial during OAE1a increased by an average factor of  
667 ~10 at the Cison and DSDP 463 sites (Fig. 2). If this OM was ~5% sulfurized, a  
668 conservative 10-fold increase in OM burial during OAE1a would yield a sulfurized-  
669 OM flux of  $\sim 3.15 \pm 0.9$  Tmol S yr<sup>-1</sup>. While enhanced reduced-S burial during OAE1a  
670 can remove most S (Fig. 8), the potentially strong input fluxes from  
671 hydrothermalism and weathering require an additional S-sink to draw seawater  
672 sulfate concentrations down to levels that support ferruginous conditions.

673         Bio-sulfur is an additional, yet often overlooked, sulfur sink that when  
674 combined with pyrite burial, is sufficiently large to draw seawater sulfate down to  
675 <600 μM. Sinks such as bio-sulfur is known to operate in low sulfate modern and  
676 ancient environments (Horner et al., 2017; Paris et al., 2014) and while bio-sulfur  
677 is a major pathway for S burial in lacustrine environments, it is often neglected in

678 the marine S cycle. Marine organisms, furthermore, assimilate S with a  $\delta^{34}\text{S}$   
679 composition nearly identical to seawater (Werne et al., 2003), and indeed, OAE1a  
680 S-isotope mass balance requires a non-reduced S-sinks (pyrite, sulfurized-OM)  
681 carry near seawater  $\delta^{34}\text{S}$  values (Fig. 8). Given the  $S_{\text{Tot}}$  and OM contents of the  
682 Cismon sediments deposited during OAE1a (Fig. 2), and assuming all non-pyrite  
683 S is buried as bio-sulfur and sulfurized-OM, we calculate C:S molar ratios between  
684 5 and 49 (average of 24), revealing that most OM buried during OAE1a has a  
685 similar C:S composition to that of modern bio-sulfur, while some of this OM was  
686 likely sulfurized. If this OM was ~5 wt% S, a conservative 10-fold increase in OM  
687 burial during OAE1a ( $\sim 3.5 \pm 0.9 \text{ Tmol S yr}^{-1}$ ) would be, together with pyrite burial  
688 ( $1.15 \pm 0.30 \text{ Tmol S yr}^{-1}$ ) and sulfurized-OM ( $3.15 \pm 0.90 \text{ Tmol S yr}^{-1}$ ), sufficient  
689 to draw the marine sulfate reservoir down to  $600 \pm 320 \mu\text{M}$  during OAE1a (Fig. 8  
690 and Fig. S7), within error of estimates from our 1D model (Fig. 6).

691 Although uncertainties in Cretaceous S-budgets and fluxes are large, our  
692 modeling estimates plausible seawater sulfate concentrations within available  
693 constraints. Importantly, our model results reproduce  $\delta^{34}\text{S}_{\text{Sulfate}}$  records and S  
694 burial fluxes in OAE1a sediments at seawater sulfate concentrations that are  
695 consistent with ferruginous conditions. The development of ferruginous conditions  
696 can, therefore, be attributed to widespread oceanic anoxia and ensuing sulfate  
697 drawdown through pelagic sulfate reduction and enhanced burial of bio-sulfur, all  
698 against the backdrop of low Cretaceous seawater sulfate concentrations, strong  
699 hydrothermalism, and weathering. Furthermore, at a seawater sulfate  
700 concentration of  $\sim 250 \mu\text{M}$  and peak S-fluxes in our mass balance model, we  
701 calculate a residence time for seawater sulfate of  $\sim 55 \text{ kyrs}$ , which is an order of  
702 magnitude longer than the modern ocean mixing time ( $\sim 3 \text{ kyrs}$ ). Relative  
703 homogeneity in Aptian  $\delta^{34}\text{S}_{\text{Sulfate}}$  records is thus expected, even with seawater  
704 sulfate concentrations well below 1 mM.

705

## 706 **5.0 Implications and conclusions**

707 At 28 mM, seawater sulfate is an oxidant pool twice the size of  
708 modern atmospheric  $\text{O}_2$ . A decline to below  $600 \mu\text{M}$  seawater sulfate

709 concentrations consequently indicates a large-scale reorganization of global  
710 oxidant pools during OAE1a with implications for marine ecology, biogeochemical  
711 cycling, and climate. Water column anoxia, for example, may have extended at  
712 least transiently into the photic zone during OAE1a with potential to influence  
713 photosynthetic ecology. Indeed, biomarkers indicative of green S-bacteria (phylum  
714 Chlorobi) have been recovered in sediments deposited during OAE1a (van  
715 Breugel et al., 2007). Preservation of biomarkers from green S-bacteria in Aptian  
716 ferruginous sediments could signal the return of photoferrotrophy to the  
717 Phanerozoic oceans, as they are known to grow on ferrous Fe (photoferrotrophy)  
718 (Crowe et al., 2008). Seawater sulfate concentrations are also an important control  
719 on marine methane (CH<sub>4</sub>) budgets, with super-millimolar sulfate concentrations  
720 attenuating the release of CH<sub>4</sub> from modern marine sediments to the atmosphere  
721 through microbial anaerobic methane oxidation (Reeburgh, 2007). Sub-millimolar  
722 sulfate concentrations, in contrast, can lead to large-scale oceanic CH<sub>4</sub> efflux with  
723 corresponding implications for climate (Olson et al., 2016). Seawater sulfate  
724 concentrations <600 μM could thus promote marine methane efflux to the  
725 atmosphere with potential greenhouse warming.

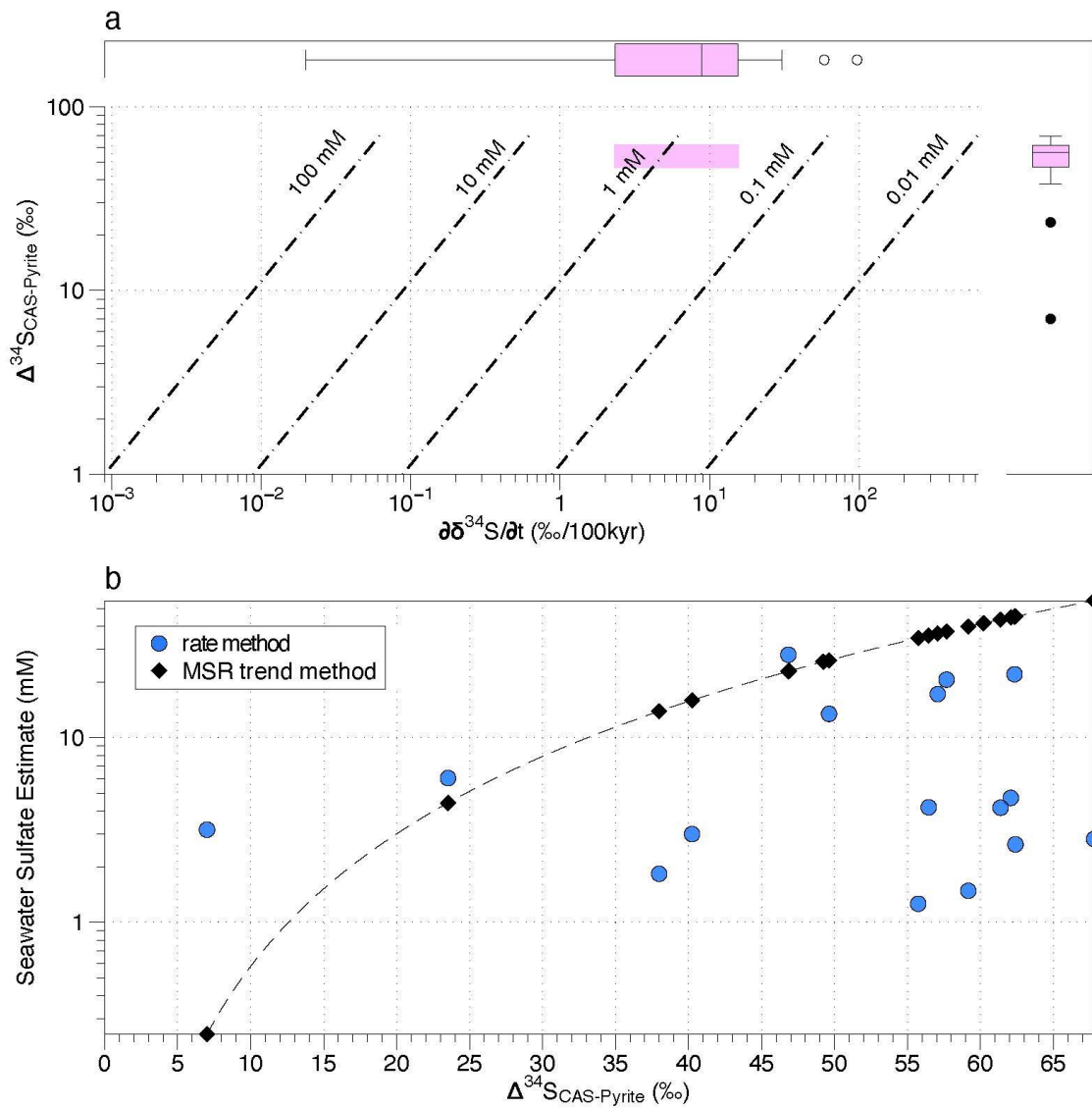
726         Development of ferruginous conditions during OAE1a reveals large-scale  
727 dynamics in Earth's biogeochemical cycles over intervals of <100 kyrs. The  
728 development of ferruginous ocean conditions during multiple OAEs may thus  
729 signify a general instability in Earth surface redox budgets and the recurrent  
730 reorganization of major oxidant pools at Earth's surface, like seawater sulfate,  
731 during the Phanerozoic Eon. In particular, emerging reconstructions of seawater  
732 sulfate concentrations during multiple Phanerozoic OAEs, suggest repeated  
733 collapse of the seawater sulfate reservoir to below 1 mM, possibly below 100 μM,  
734 over short timescales (<50 kyrs) (He et al., 2020). The mechanisms driving this  
735 reorganization remain uncertain but could be addressed through better constraints  
736 on global S-budgets and the drivers of ocean deoxygenation, as well as Earth  
737 system modeling that resolves such biogeochemical dynamics over relatively short  
738 time scales.

739



740  
741  
742  
743  
744  
745  
746  
747  
748

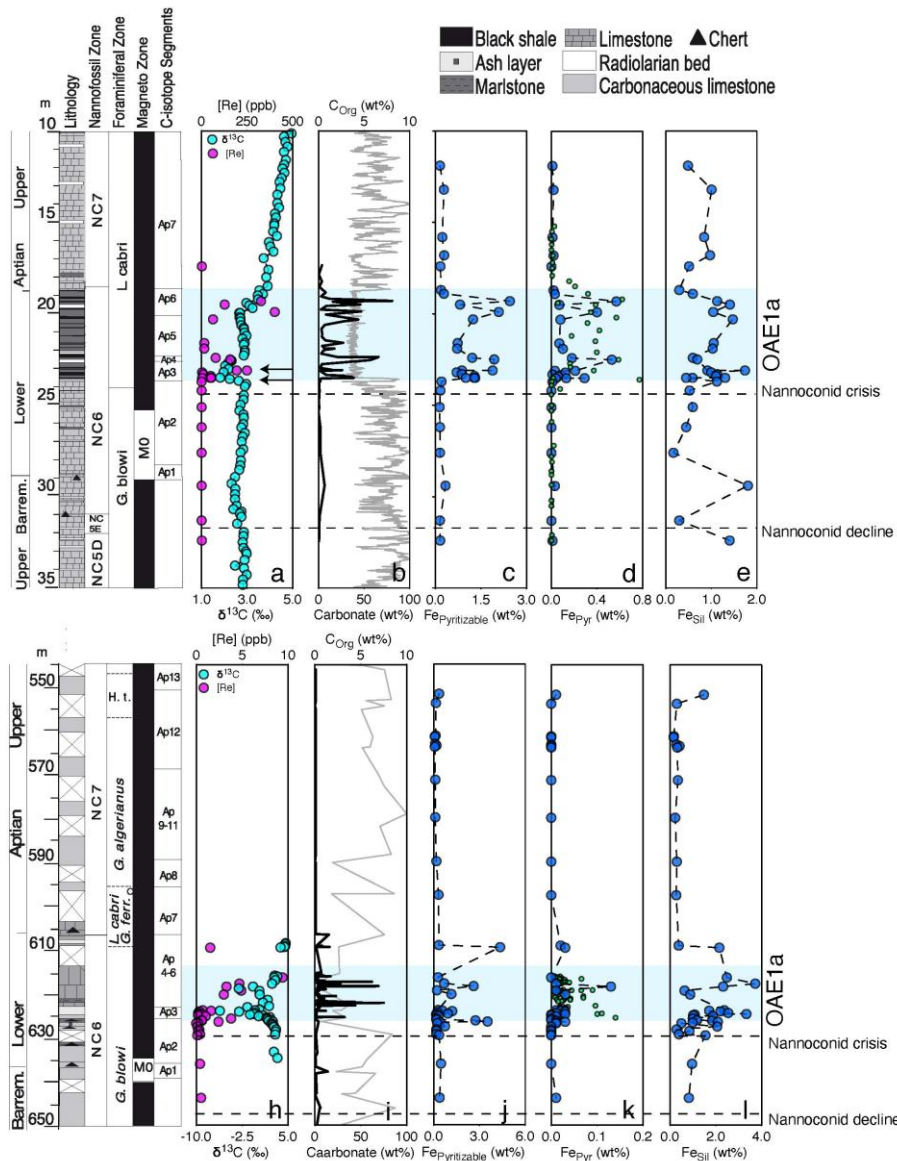
**Figures and captions**



749  
750  
751  
752

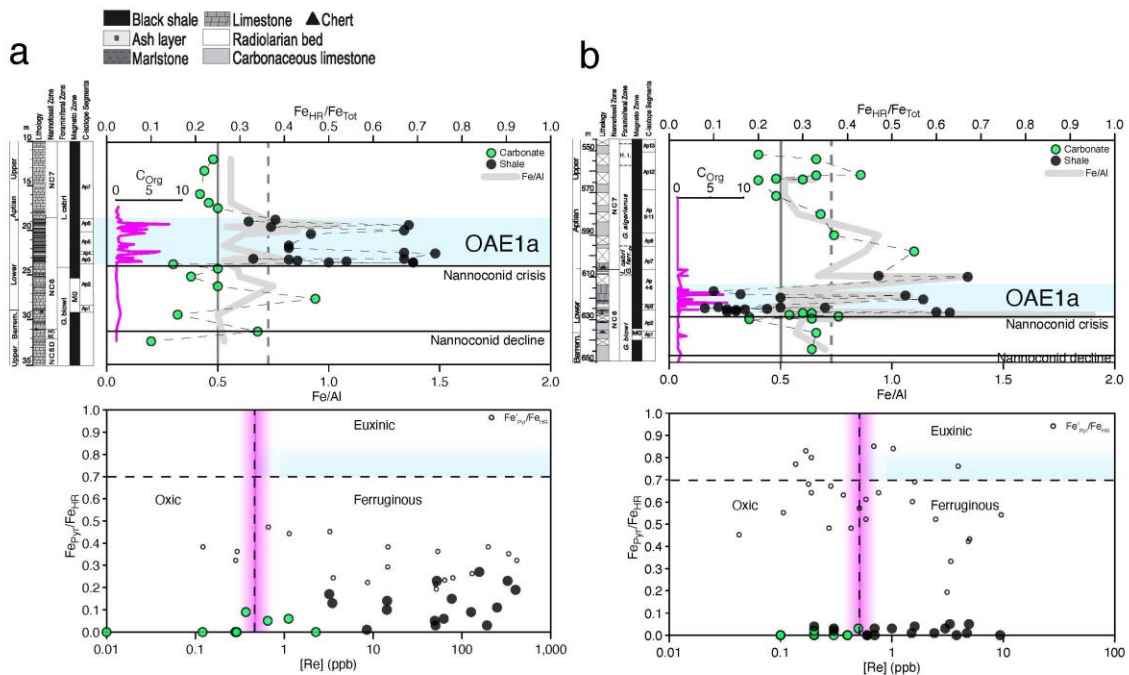
**Figure 1. (a)** Rate method estimates for early Aptian seawater sulfate concentrations using the approach presented in (Algeo et al., 2015). Seawater sulfate concentrations were calculated using a S-pyrite burial flux of  $1.3 \times 10^{12}$  mol  $\text{yr}^{-1}$ . The x-axis box and

753 whisker plot represent  $\partial \delta^{34}\text{S}_{\text{Sulfate}} / \partial t$  calculated using Aptian S-isotope data from  
 754 (Gomes et al., 2016; Kristall et al., 2018; Mills et al., 2017). The y-axis box and whisker  
 755 plot represents  $\Delta^{34}\text{S}_{\text{Sulfate-Pyrite}}$  from (Gomes et al., 2016; Kristall et al., 2018; Mills et al.,  
 756 2017) The pink shaded region represents the parameter space where the ranges between  
 757 the 25<sup>th</sup> and 75<sup>th</sup> percentiles of the  $\Delta^{34}\text{S}_{\text{CAS}}$  and  $\partial \delta^{34}\text{S}_{\text{Sulfate}} / \partial t$  distributions overlap,  
 758 corresponding to a likely range of range of seawater sulfate estimates. **(b)** All data points  
 759 represent paired cogenetic S-isotope data for Aptian sulfate ( $\delta^{34}\text{S}_{\text{Sulfate}}$ ) and sulfide  
 760 ( $\delta^{34}\text{S}_{\text{Pyrite}}$ ) (Gomes et al., 2016). For the rate method, seawater sulfate concentrations were  
 761 calculated using a S-pyrite burial flux of  $1.3 \times 10^{12} \text{ mol yr}^{-1}$ . For the MSR trend method, the  
 762 values were calculated using the relationship presented in (Algeo et al., 2015)  
 763 (Supplementary Information).  
 764



765  
 766 **Figure 2.** Fe-speciation and carbon isotope records for Cison and DSDP Site 463 cores.  
 767 Integrated stratigraphy of the Cison and DSDP Site 463 after (Bottini et al., 2015; Erba  
 768 et al., 2010). The grey shaded region (OAE1a) represents ~1.1 Myrs (Malinverno et al.,

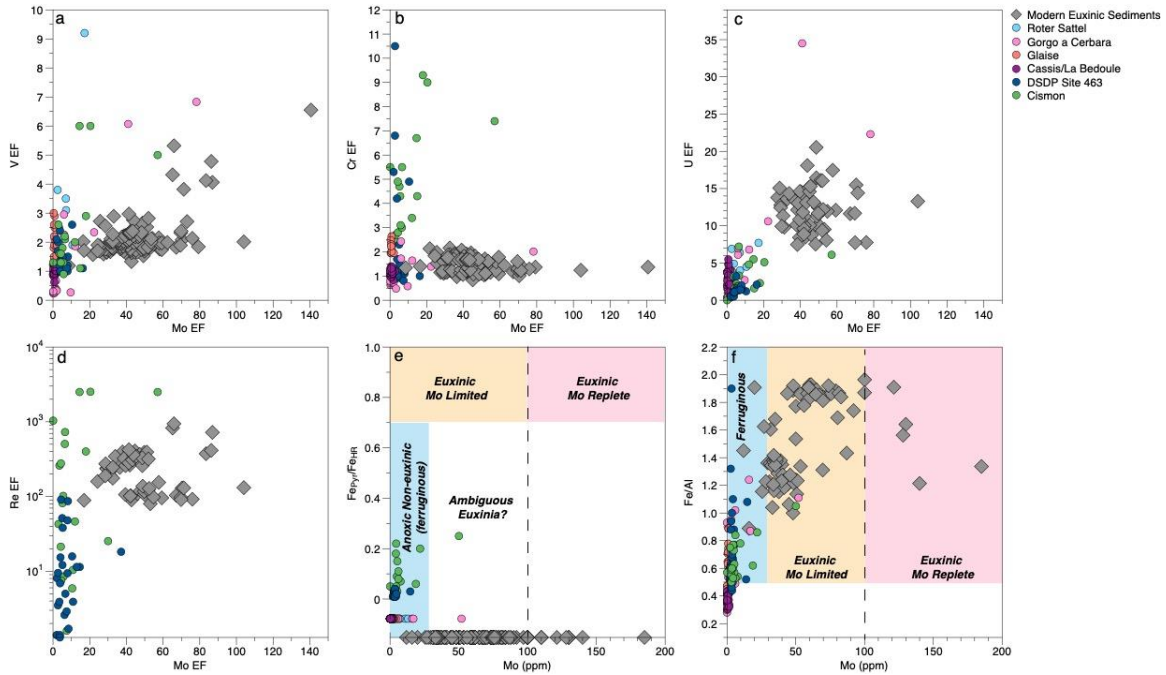
769 2010), C-isotope stages C2–C7 (Bottini et al., 2015). Panels (a-e) are Cismon data and  
 770 panels (f-j) are DSDP Site 463 data. **(a)** Cismon C-isotope data from (Bottini et al., 2015).  
 771 Rhenium concentration data from (Bottini et al., 2012). **(b)** Carbonate C, and organic  
 772 matter C data after (Bottini et al., 2012; Bottini et al., 2015). **(c)**  $Fe_{Pyritizable}$ ; sum of all  
 773 pyritizable  $Fe_{HR}$  pools ( $Fe_{Carb}$ ,  $Fe_{OM}$ ,  $Fe_{Ox}$ ) **(d)**  $Fe_{Sil}$ ; silicate Fe **(e)**  $Fe_{Pyr}$ ; pyrite Fe. Green  
 774 data represent pyrite concentration data from (Gomes et al., 2016). **(f)** DSDP Site 463 C-  
 775 isotope data from (Bottini et al., 2012). Rhenium concentration data from (Bottini et al.,  
 776 2012). **(g)** Carbonate C data from (Bottini et al., 2015), organic C data from (Bottini et al.,  
 777 2015; van Breugel et al., 2007). **(h)**  $Fe_{Pyritizable}$ ; sum of all pyritizable  $Fe_{HR}$  pools ( $Fe_{Carb}$ ,  
 778  $Fe_{OM}$ ,  $Fe_{Ox}$ ) **(i)**  $Fe_{Sil}$ ; silicate Fe. **(j)**  $Fe_{Pyr}$ ; pyrite Fe. Green data represent pyrite  
 779 concentration estimates from (Mélières et al., 1981). The start of the nannoconid decline  
 780 and beginning of the nannoconid crisis are marked with dashed lines (Erba et al., 2010).



781 **Figure 3. (a)** Fe-speciation and Fe/Al records of the Cismon and DSDP Site 463 **(b)**. The  
 782 vertical and horizontal dotted lines refer to the oxic-anoxic threshold ( $Fe_{HR}/Fe_{Tot} = 0.38$ )  
 783 and a conservative ferruginous-euxinic threshold ( $Fe_{Pyr}/Fe_{HR} = 0.70$ ), respectively. The  
 784 open circles represent  $Fe_{Pyr}/Fe_{HR}$ , the amount of pyrite present in the samples assuming  
 785 the unlikely scenario where the entire  $Fe_{Ox}$  pool is a result of  $Fe_{Pyr}$  oxidation. The solid  
 786 vertical line in the top panels refers to the  $Fe/Al$  ratio of 0.5. The solid vertical line in the  
 787 bottom panels refers to the average rhenium concentration of the PAAS, with the purple  
 788 shading representing a 2 sigma uncertainty on this value (McLennan, 2001). Litho-, bio-  
 789 and magneto-stratigraphy is the same as Figure 1.

791  
 792  
 793  
 794  
 795  
 796  
 797  
 798  
 799

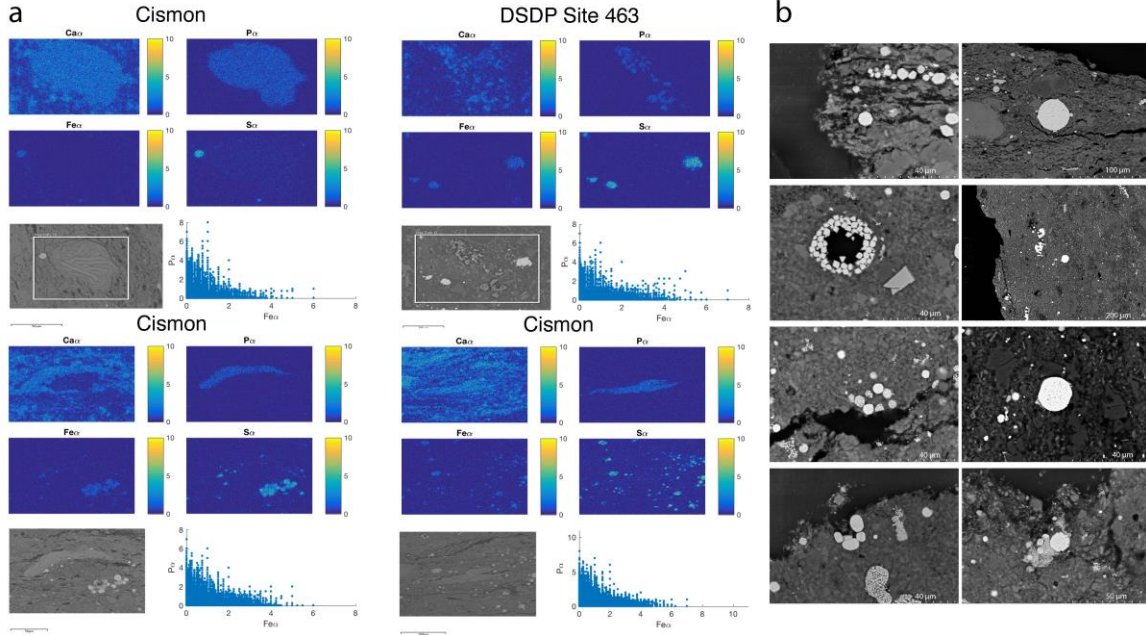
800  
801  
802  
803  
804  
805  
806  
807  
808  
809  
810



811  
812  
813  
814  
815  
816  
817  
818  
819  
820  
821  
822  
823  
824  
825  
826  
827  
828  
829  
830  
831

**Figure 4.** RSTE enrichment factors (EFs) and molybdenum concentrations. EFs were calculated by normalizing to the PAAS. Data from other OAE1a sedimentary sections as follows; Gorgo a Cerbara, Glaise, and Cassis la Bédoule (Follmi, 2012; Westermann et al., 2013), Roter Sattel (Charbonnier et al., 2018). All modern environment RSTE data come from hydrologically restricted euxinic basins (Bennett and Canfield, 2020). **(a)** V EFs vs Mo EFs. **(b)** Cr EFs vs. Mo EFs. **(c)** U EFs vs. Mo EFs. **(d)** Re EFs vs. Mo EFs. **(e)**  $Fe_{Pyr}/Fe_{HR}$  vs. Mo concentrations. The data for other OAE1a sections and modern environments do not have corresponding  $Fe_{Pyr}$  values and thus these data plot on the x-axis. All OAE1a data points (2 analyses excepted) exhibit Mo concentrations that unambiguously demonstrate non-euxinic conditions. **(f)** Fe/Al vs. Mo concentrations. Fe/Al ratios  $>0.5$  imply anoxic conditions (Lyons and Severmann, 2006). All OAE1a data points that plot above this threshold (2 analyses excepted) exhibit Mo concentrations that unambiguously demonstrate ferruginous (non-euxinic) conditions.

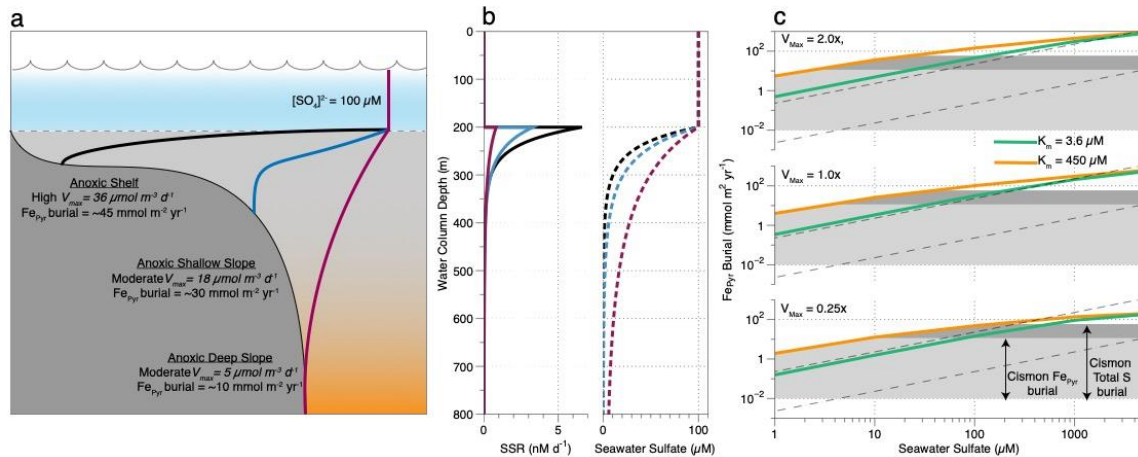
832  
833



834  
835 **Figure 5. (a)** SEM-EDS analyses of Ca-P bearing minerals (apatite) in the Cision and  
836 DSDP Site 463 sediments. We observe a tight coupling between the distribution of Ca and  
837 P in the OAE1a samples, and no relationship between the distribution of Fe and P,  
838 implying no redistribution of P into freshly formed poorly crystalline Fe-(oxyhydr)oxide  
839 phases and a lack of the pyrite oxidation mechanism observed by Kraal et al. (2009). **(b)**  
840 Compilation of back scatter electron (BSE) SEM images obtained on thin sections of  
841 OAE1a samples from both the Cision and DSDP Site 463 sediments. We observe no  
842 strong evidence for pyrite/marcasite oxidation, even on crystals located near thin section  
843 boundaries where oxidation would be most concentrated.

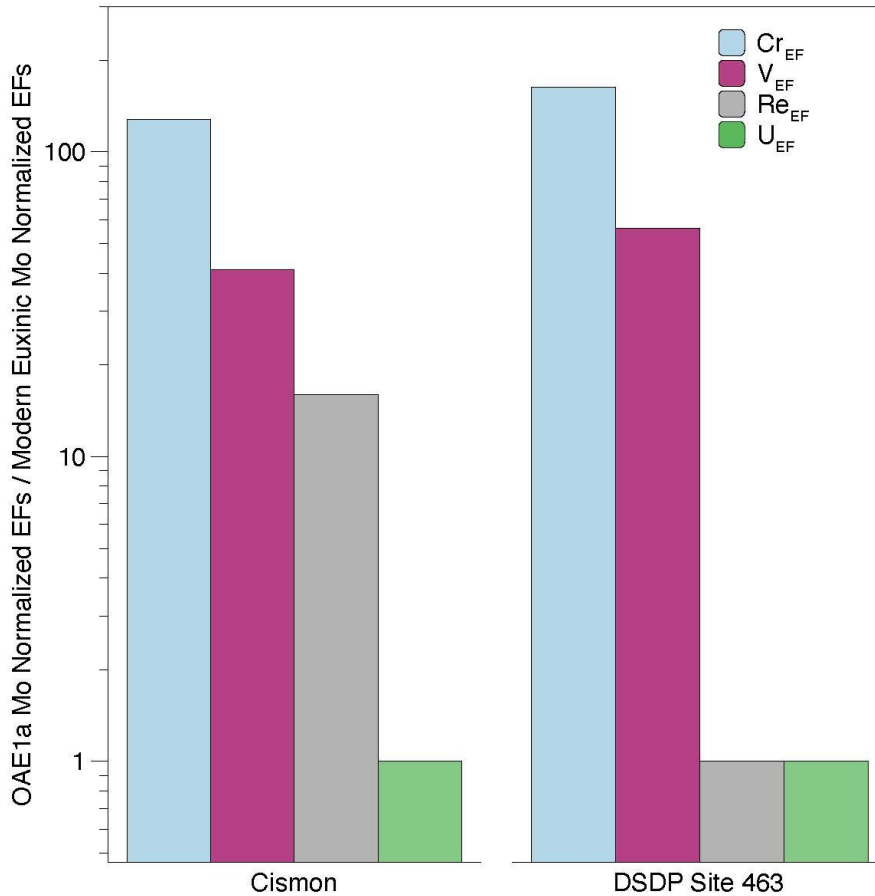
844  
845  
846  
847  
848  
849  
850  
851  
852  
853  
854  
855  
856  
857  
858  
859  
860  
861  
862  
863  
864





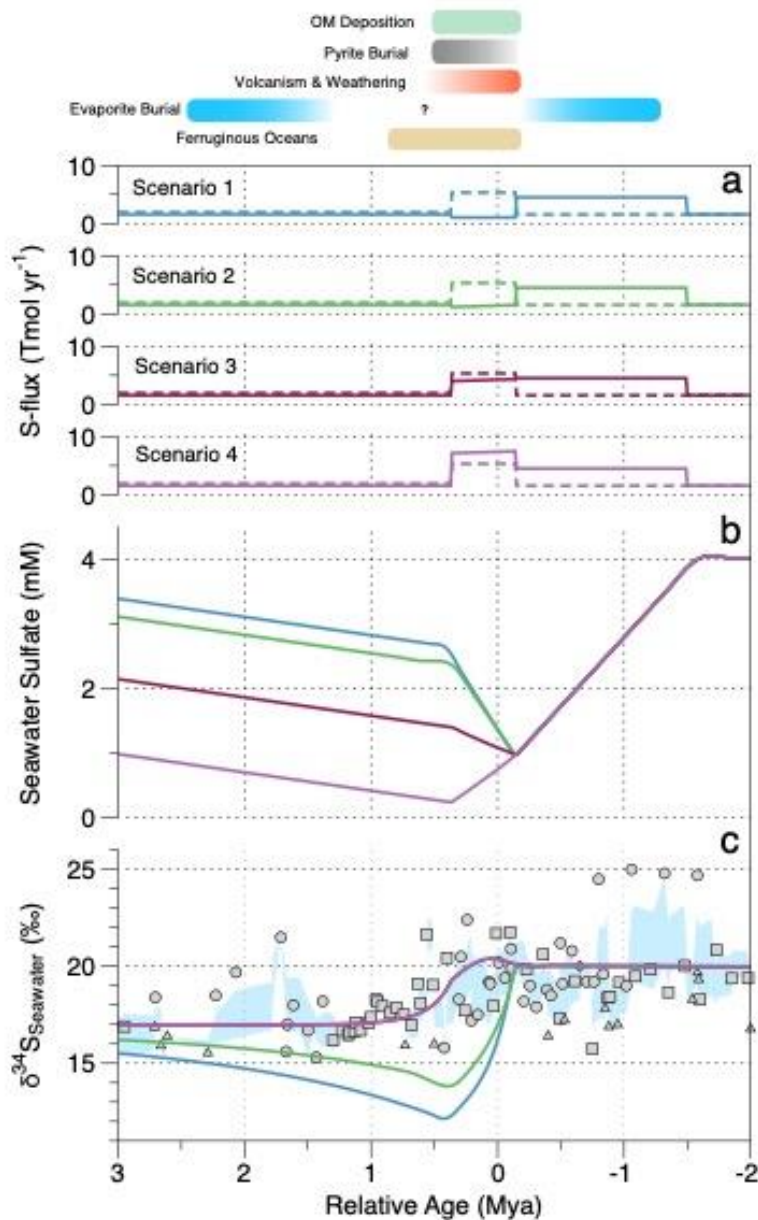
865  
866  
867  
868  
869  
870  
871  
872  
873  
874  
875  
876  
877  
878  
879  
880  
881  
882  
883  
884  
885  
886  
887  
888  
889  
890  
891  
892  
893  
894  
895

**Figure 6.** 1D water column reaction transport model sensitivity analyses. **(a)** Schematic model representation of a stratified Cretaceous water column. The model is designed such that seawater sulfate must be exhausted by the bottom of the domain (sediment-water interface) under anoxic conditions via sulfate reduction promoting the development of ferruginous conditions. **(b)** Sulfate reduction rates and resulting seawater sulfate concentrations under different parameterizations of  $V_{max}$ . **(c)** Water column depth integrated sulfate reduction rates (pyrite burial). The data points represent different model outputs for the indicated scenarios. The solid black lines (equation =  $[\text{SO}_4^{2-}]/\partial z * K_z$ ) mark the pyrite burial rates needed to support complete drawdown of sulfate at a given surface seawater sulfate concentration. The lower line corresponds to a  $K_z = 0.01 \text{ m}^2 \text{ d}^{-1}$  and the upper line corresponds to a  $K_z = 1 \text{ m}^2 \text{ d}^{-1}$ . The only allowable model runs thus need to plot above these lines. The light grey shading corresponds to the allowable parameter space that satisfies both the requirement for complete sulfate drawdown and the conservative condition for local pyrite burial rates to be less than  $10 \text{ mmol m}^{-2} \text{ yr}^{-1}$ . The dark grey shading corresponds to the allowable parameter space that satisfies both the requirement for complete sulfate drawdown and the conservative condition for local  $\text{S}_{\text{Tot}}$  burial rates to be less than the conservative maximum of  $60 \text{ mmol m}^{-2} \text{ yr}^{-1}$ . Maximum allowable sulfate concentrations come from extending a vertical line to the x-axis at point of intersection between the model outputs (green and orange lines) and the shaded regions.



896  
897  
898  
899  
900  
901  
902  
903  
904  
905  
906  
907  
908  
909  
910  
911  
912  
913  
914  
915  
916  
917

**Figure 7.** OAE1a RSTE enrichment factors (EFs) compared to modern euxinic sediments. Displayed are EFs of RSTEs normalized to Mo enrichment factor in the OAE1a sediments compared to RSTE EFs normalized to Mo in example modern euxinic basins;  $\frac{(OAE1a \frac{RSTE_{EF}}{Mo_{EF}})}{(Modern Euxinic \frac{RSTE_{EF}}{Mo_{EF}})}$ . We find that the RSTE enrichment factors of Cr, V, and Re, metals that do not require sulfide to be buried under anoxic conditions, are dramatically enriched in both the Cison and DSDP 463 sediments, relative to modern euxinic basins. Modern data is from (Bennett and Canfield, 2020).



918  
 919 **Figure 8.** Evolution of the Cretaceous seawater sulfate reservoir. The coloured bars  
 920 represent the conceptual model and proposed timing of early Cretaceous events  
 921 associated with the development of OAE1a. **(a)** S-input (dashed lines) and output (solid  
 922 lines) fluxes. *Scenario 1*: 6.6x evaporite burial 1 Myr followed by 4.2x hydrothermal + 3x  
 923 weathering fluxes for 0.5 Myr. *Scenario 2*: Scenario 1 + 1.75x pyrite burial. *Scenario 3*:  
 924 Scenario 2 + 10x bio-sulfur burial. *Scenario 4*: Scenario 3 + 10x sulfurized-OM burial. **(b)**  
 925 Resulting seawater sulfate concentrations for each scenario in (a). **(c)** Modelled  $\delta^{34}\text{S}_{\text{sulfate}}$   
 926 under for scenario in (a). Aptian  $\delta^{34}\text{S}$  data as follows; circles (Gomes et al., 2016), squares  
 927 (Mills et al., 2017), triangles (Kristall et al., 2018), diamonds (Paytan et al., 2004). The blue  
 928 shading represents a 5-point  $\delta^{34}\text{S}$  moving average of all data using a 2s.d. error envelope.  
 929

930

931

932

## Acknowledgements



933

934 This work was funded through NSERC Discovery Grants to Sean A. Crowe (0487)  
935 and Roger Francois, the Canadian Foundation for Innovation, the Canada  
936 Research Chairs Program, and a UBC 4-Year Fellowship to Kohen W. Bauer. EE  
937 and CB were funded by PRIN 2017RX9XXY to EE. We thank the International  
938 Ocean Discovery Program (IODP) for providing the DSDP Site 463 samples. We  
939 thank John Greenough for help with the milling of rock samples. We also  
940 acknowledge Steve Calvert for participating in helpful discussions on rhenium  
941 geochemistry.

942

#### 943 **Data availability statement**

944

945 The datasets and models generated during and/or analysed during the current  
946 study are available from the corresponding author on reasonable request.

947

#### 948 **CRedit author statement**

949

950 **KWB:** validation, formal analysis, investigation, data curation, writing,  
951 visualization. **CB:** resources, data curation, visualization, validation, writing. **SK:**  
952 validation, software, methodology, formal analysis, writing. **MJ:** validation, writing.  
953 **RF:** conceptualization, validation, supervision, funding acquisition, writing. **EE:**  
954 resources, visualization, validation, writing. **SAC:** conceptualization, validation,  
955 supervision, project administration, funding acquisition, writing.

956

#### 957 **References**

958

- 959 Algeo, T.J., Luo, G.M., Song, H.Y., Lyons, T.W., Canfield, D.E., 2015. Reconstruction of  
960 secular variation in seawater sulfate concentrations. *Biogeosciences* 12, 2131-2151.
- 961 Bennett, W.W., Canfield, D.E., 2020. Redox-sensitive trace metals as paleoredox  
962 proxies: A review and analysis of data from modern sediments. *Earth-Sci. Rev.* 204.
- 963 Berner, R.A., 1981. A new geochemical classification of sedimentary environments.  
964 *Journal of Sedimentary Research* 51, 359-365.
- 965 Bottini, C., Cohen, A.S., Erba, E., Jenkyns, H.C., Coe, A.L., 2012. Osmium-isotope  
966 evidence for volcanism, weathering, and ocean mixing during the early Aptian OAE  
967 1a. *Geology* 40, 583-586.
- 968 Bottini, C., Erba, E., Tiraboschi, D., Jenkyns, H., Schouten, S., Sinninghe Damsté, J.,  
969 2015. Climate variability and ocean fertility during the Aptian Stage. *Climate of the*  
970 *Past* 11, 383-402.
- 971 Canfield, D.E., Boudreau, B.P., Mucci, A., Gundersen, J.K., 1998. The early diagenetic  
972 formation of organic sulfur in the sediments of Mangrove Lake, Bermuda.  
973 *Geochimica et Cosmochimica Acta* 62, 767-781.
- 974 Canfield, D.E., Farquhar, J., 2012. The global sulfur cycle. *Fundamentals of*  
975 *geobiology*, 49-64.
- 976 Chaboureaud, A.C., Guillocheau, F., Robin, C., Rohais, S., Moulin, M., Aslanian, D., 2013.  
977 Paleogeographic evolution of the central segment of the South Atlantic during Early

978 Cretaceous times: Paleotopographic and geodynamic implications. *Tectonophysics*  
979 604, 191-223.

980 Charbonnier, G., Adatte, T., Spangenberg, J.E., Follmi, K.B., 2018. The expression of  
981 early Aptian to latest Cenomanian oceanic anoxic events in the sedimentary record  
982 of the Briançonnais domain. *Global and Planetary Change* 170, 76-92.

983 Chen, C.T.A., Lin, C.M., Huang, B.T., Chang, L.F., 1996. Stoichiometry of carbon,  
984 hydrogen, nitrogen, sulfur and oxygen in the particulate matter of the western North  
985 Pacific marginal seas. *Marine Chemistry* 54, 179-190.

986 Crowe, S.A., Jones, C., Katsev, S., Magen, C., O'Neill, A.H., Sturm, A., Canfield, D.E.,  
987 Haffner, G.D., Mucci, A., Sundby, B., Fowle, D.A., 2008. Photoferrotrophs thrive in an  
988 Archean Ocean analogue. *Proceedings of the National Academy of Sciences of the*  
989 *United States of America* 105, 15938-15943.

990 Crowe, S.A., Paris, G., Katsev, S., Jones, C., Kim, S.-T., Zerkle, A.L., Nomosatryo, S.,  
991 Fowle, D.A., Adkins, J.F., Sessions, A.L., Farquhar, J., Canfield, D.E., 2014. Sulfate was a  
992 trace constituent of Archean seawater. *Science* 346, 735-739.

993 Damste, J.S.S., Koster, J., 1998. A euxinic southern North Atlantic Ocean during the  
994 Cenomanian/Turonian oceanic anoxic event. *Earth and Planetary Science Letters*  
995 158, 165-173.

996 Davison, I., 2007. *Geology and tectonics of the South Atlantic Brazilian salt basins.*  
997 Geological Society, London, Special Publications 272, 345-359.

998 Eglinton, T.I., Irvine, J.E., Vairavamurthy, A., Zhou, W., Manowitz, B., 1994. Formation  
999 and diagenesis of macromolecular organic sulfur in Peru margin sediments. *Organic*  
1000 *Geochemistry* 22, 781-799.

1001 Erba, E., Bottini, C., Weissert, H.J., Keller, C.E., 2010. Calcareous Nannoplankton  
1002 Response to Surface-Water Acidification Around Oceanic Anoxic Event 1a. *Science*  
1003 329, 428-432.

1004 Fagerbakke, K.M., Heldal, M., Norland, S., 1996. Content of carbon, nitrogen, oxygen,  
1005 sulfur and phosphorus in native aquatic and cultured bacteria. *Aquatic Microbial*  
1006 *Ecology* 10, 15-27.

1007 Follmi, K.B., 2012. Early Cretaceous life, climate and anoxia. *Cretaceous Research* 35,  
1008 230-257.

1009 Francois, R., 1987. A study of sulphur enrichment in the humic fraction of marine  
1010 sediments during early diagenesis. *Geochimica et Cosmochimica Acta* 51, 17-27.

1011 Gomes, M.L., Hurtgen, M.T., Sageman, B.B., 2016. Biogeochemical sulfur cycling  
1012 during Cretaceous oceanic anoxic events: A comparison of OAE1a and OAE2.  
1013 *Paleoceanography* 31, 233-251.

1014 Hansen, K.W., Wallmann, K., 2003. Cretaceous and Cenozoic evolution of seawater  
1015 composition, atmospheric O<sub>2</sub> and CO<sub>2</sub>: a model perspective. *Am. J. Sci.* 303, 94-148.

1016 Hardisty, D.S., Lyons, T.W., Riedinger, N., Isson, T.T., Owens, J.D., Aller, R.C., Rye, D.M.,  
1017 Planavsky, N.J., Reinhard, C.T., Gill, B.C., 2018. An evaluation of sedimentary  
1018 molybdenum and iron as proxies for pore fluid paleoredox conditions. *Am. J. Sci.*  
1019 318, 527-556.

1020 Hartnett, H.E., Devol, A.H., 2003. Role of a strong oxygen-deficient zone in the  
1021 preservation and degradation of organic matter: A carbon budget for the continental  
1022 margins of northwest Mexico and Washington State. *Geochimica Et Cosmochimica*  
1023 *Acta* 67, 247-264.

1024 He, T., Dal Corso, J., Newton, R.J., Wignall, P.B., Mills, B.J., Todaro, S., Di Stefano, P.,  
1025 Turner, E.C., Jamieson, R.A., Randazzo, V., 2020. An enormous sulfur isotope  
1026 excursion indicates marine anoxia during the end-Triassic mass extinction. *Science*  
1027 *Advances* 6, eabb6704.

1028 Horner, T.J., Pryer, H.V., Nielsen, S.G., Crockford, P.W., Gauglitz, J.M., Wing, B.A.,  
1029 Ricketts, R.D., 2017. Pelagic barite precipitation at micromolar ambient sulfate.  
1030 *Nature Communications* 8.

1031 Jellinek, A., Lenardic, A., Pierrehumbert, R., 2020. Ice, fire, or fizzle: The climate  
1032 footprint of Earth's supercontinental cycles. *Geochemistry, Geophysics, Geosystems*  
1033 21, e2019GC008464.

1034 Jenkyns, H.C., 2010. Geochemistry of oceanic anoxic events. *Geochemistry*  
1035 *Geophysics Geosystems* 11, 30.

1036 Kraal, P., Slomp, C.P., Forster, A., Kuypers, M.M.M., Sluijs, A., 2009. Pyrite oxidation  
1037 during sample storage determines phosphorus fractionation in carbonate-poor  
1038 anoxic sediments. *Geochimica Et Cosmochimica Acta* 73, 3277-3290.

1039 Kristall, B., Jacobson, A.D., Sageman, B.B., Hurtgen, M.T., 2018. Coupled strontium-  
1040 sulfur cycle modeling and the Early Cretaceous sulfur isotope record.  
1041 *Palaeogeography Palaeoclimatology Palaeoecology* 496, 305-322.

1042 Luther III, G.W., Giblin, A., Howarth, R.W., Ryans, R.A., 1982. Pyrite and oxidized iron  
1043 mineral phases formed from pyrite oxidation in salt marsh and estuarine sediments.  
1044 *Geochimica et Cosmochimica Acta* 46, 2665-2669.

1045 Lyons, T.W., Severmann, S., 2006. A critical look at iron paleoredox proxies: New  
1046 insights from modern euxinic marine basins. *Geochimica Et Cosmochimica Acta* 70,  
1047 5698-5722.

1048 Malinverno, A., Erba, E., Herbert, T.D., 2010. Orbital tuning as an inverse problem:  
1049 Chronology of the early Aptian oceanic anoxic event 1a (Selli Level) in the Cismon  
1050 APTICORE. *Paleoceanography* 25.

1051 Martin, J.H., Knauer, G.A., Karl, D.M., Broenkow, W.W., 1987. VERTEX: carbon cycling  
1052 in the northeast Pacific. *Deep Sea Research Part A. Oceanographic Research Papers*  
1053 34, 267-285.

1054 Marz, C., Poulton, S.W., Beckmann, B., Kuster, K., Wagner, T., Kasten, S., 2008. Redox  
1055 sensitivity of P cycling during marine black shale formation: Dynamics of sulfidic  
1056 and anoxic, non-sulfidic bottom waters. *Geochimica Et Cosmochimica Acta* 72, 3703-  
1057 3717.

1058 McAnena, A., 2011. The reactivity and isotopic fractionation of Fe-bearing minerals  
1059 during sulfidation: an experimental approach. Newcastle University.

1060 McLennan, S.M., 2001. Relationships between the trace element composition of  
1061 sedimentary rocks and upper continental crust. *Geochemistry Geophysics*  
1062 *Geosystems* 2, art. no.-2000GC000109.

1063 Mélières, F., Deroo, G., Herbin, J.-P., 1981. Organic-matter-rich and hypersiliceous  
1064 Aptian sediments from Western Mid-Pacific Mountains, Deep Sea Drilling Project  
1065 Leg 62, Initial Reports of the Deep Sea Drilling Project. U.S. Govt. Printing Office.

1066 Mills, J.V., Gomes, M.L., Kristall, B., Sageman, B.B., Jacobson, A.D., Hurtgen, M.T., 2017.  
1067 Massive volcanism, evaporite deposition, and the chemical evolution of the Early  
1068 Cretaceous ocean. *Geology* 45, 475-478.

1069 Munk, W., Wunsch, C., 1998. Abyssal recipes II: Energetics of tidal and wind mixing.  
1070 Deep Sea Research Part I: Oceanographic Research Papers 45, 1977-2010.  
1071 Olson, S.L., Reinhard, C.T., Lyons, T.W., 2016. Limited role for methane in the mid-  
1072 Proterozoic greenhouse. Proceedings of the National Academy of Sciences of the  
1073 United States of America 113, 11447-11452.  
1074 Paris, G., Adkins, J.F., Sessions, A.L., Webb, S.M., Fischer, W.W., 2014. Neoproterozoic  
1075 carbonate-associated sulfate records positive  $\Delta S_{33}$  anomalies. Science 346,  
1076 739-741.  
1077 Pasquier, V., Bryant, R., Fike, D., Halevy, I., 2021. Strong local, not global, controls on  
1078 marine pyrite sulfur isotopes. Science Advances 7, eabb7403.  
1079 Paytan, A., Kastner, M., Campbell, D., Thieme, M.H., 2004. Seawater sulfur isotope  
1080 fluctuations in the Cretaceous. Science 304, 1663-1665.  
1081 Poulton, S.W., Canfield, D.E., 2005. Development of a sequential extraction  
1082 procedure for iron: implications for iron partitioning in continentally derived  
1083 particulates. Chemical Geology 214, 209-221.  
1084 Poulton, S.W., Canfield, D.E., 2006. Co-diagenesis of iron and phosphorus in  
1085 hydrothermal sediments from the southern East Pacific Rise: Implications for the  
1086 evaluation of paleoseawater phosphate concentrations. Geochimica et  
1087 Cosmochimica Acta 70, 5883-5898.  
1088 Poulton, S.W., Canfield, D.E., 2011. Ferruginous Conditions: A Dominant Feature of  
1089 the Ocean through Earth's History. Elements 7, 107-112.  
1090 Poulton, S.W., Henkel, S., Marz, C., Urquhart, H., Fogel, S., Kasten, S., Damste, J.S.S.,  
1091 Wagner, T., 2015. A continental-weathering control on orbitally driven redox-  
1092 nutrient cycling during Cretaceous Oceanic Anoxic Event 2. Geology 43, 963-966.  
1093 Present, T.M., Gutierrez, M., Paris, G., Kerans, C., Grotzinger, J.P., Adkins, J.F., 2019.  
1094 Diagenetic controls on the isotopic composition of carbonate-associated sulfate  
1095 in the Permian Capitan Reef Complex, West Texas. Sedimentology 66, 2605-2626.  
1096 Raiswell, R., Hardisty, D.S., Lyons, T.W., Canfield, D.E., Owens, J.D., Planavsky, N.J.,  
1097 Poulton, S.W., Reinhard, C.T., 2018. The iron paleoredox proxies: A guide to the  
1098 pitfalls, problems and proper practice. Am. J. Sci. 318, 491-526.  
1099 Raven, M., Keil, R.G., Webb, S.M., 2021. Rapid, concurrent formation of organic sulfur  
1100 and iron sulfides during experimental sulfurization of sinking marine particles.  
1101 Global Biogeochemical Cycles, e2021GB007062.  
1102 Raven, M.R., Fike, D.A., Gomes, M.L., Webb, S.M., Bradley, A.S., McClelland, H.L.O.,  
1103 2018. Organic carbon burial during OAE2 driven by changes in the locus of organic  
1104 matter sulfurization. Nature Communications 9.  
1105 Reeburgh, W.S., 2007. Oceanic methane biogeochemistry. Chemical Reviews 107,  
1106 486-513.  
1107 Shinar, L., Halevy, I., Said-Ahmad, W., Feinstein, S., Boyko, V., Kamysny, A., Amrani,  
1108 A., 2018. Dynamics of pyrite formation and organic matter sulfurization in organic-  
1109 rich carbonate sediments. Geochimica et Cosmochimica Acta 241, 219-239.  
1110 Stolper, D.A., Keller, C.B., 2018. A record of deep-ocean dissolved  $O_2$  from the  
1111 oxidation state of iron in submarine basalts. Nature 553, 323-327.  
1112 Tedeschi, L.R., Jenkyns, H.C., Robinson, S.A., Sanjines, A.E.S., Viviers, M.C., Quintaes,  
1113 C., Vazquez, J.C., 2017. New age constraints on Aptian evaporites and carbonates

1114 from the South Atlantic: Implications for Oceanic Anoxic Event 1a. *Geology* 45, 543-  
1115 546.

1116 Timofeeff, M.N., Lowenstein, T.K., da Silva, M.A., Harris, N.B., 2006. Secular variation  
1117 in the major-ion chemistry of seawater: Evidence from fluid inclusions in Cretaceous  
1118 halites. *Geochimica Et Cosmochimica Acta* 70.

1119 Tribouvillard, N., Algeo, T.J., Lyons, T., Riboulleau, A., 2006. Trace metals as  
1120 paleoredox and paleoproductivity proxies: An update. *Chemical Geology* 232, 12-32.

1121 van Breugel, Y., Schouten, S., Tsikos, H., Erba, E., Price, G.D., Damste, J.S.S., 2007.  
1122 Synchronous negative carbon isotope shifts in marine and terrestrial biomarkers at  
1123 the onset of the early Aptian oceanic anoxic event 1a: Evidence for the release of C-  
1124 13-depleted carbon into the atmosphere. *Paleoceanography* 22.

1125 Werne, J.P., Lyons, T.W., Hollander, D.J., Formolo, M.J., Damsté, J.S.S., 2003. Reduced  
1126 sulfur in euxinic sediments of the Cariaco Basin: sulfur isotope constraints on  
1127 organic sulfur formation. *Chemical Geology* 195, 159-179.

1128 Westermann, S., Stein, M., Matera, V., Fiet, N., Fleitmann, D., Adatte, T., Foellmi, K.B.,  
1129 2013. Rapid changes in the redox conditions of the western Tethys Ocean during the  
1130 early Aptian oceanic anoxic event. *Geochimica Et Cosmochimica Acta* 121, 467-486.

1131 Wortmann, U.G., Chernyavsky, B.M., 2007. Effect of evaporite deposition on Early  
1132 Cretaceous carbon and sulphur cycling. *Nature* 446, 654-656.

1133